JGR Atmospheres

RESEARCH ARTICLE
10.1029/2020JD034509

Impacts of Urban Canopy on Two Convective Storms With Contrasting Synoptic Conditions Over Nanjing, China

Long Yang[1], Qi Li[2], Huiling Yuan[3], Zhixing Niu[4], and Lachun Wang[1]

[1]School of Geography and Ocean Science, Nanjing University, Nanjing, Jiangsu, China, [2]School of Civil and Environmental Engineering, Cornell University, Ithaca, NY, USA, [3]School of Atmospheric Science, Nanjing University and Key Laboratory of Mesoscale Severe Weather, Ministry of Education, Nanjing, Jiangsu, China, [4]Nanjing Automation Institute of Water Conservancy and Hydrology, Ministry of Water Resources, Nanjing, Jiangsu, China

Key Points:

- A high-resolution data set of urban canopy parameters is developed to examine the impacts of urban canopy on rainfall variabilities
- Contrasting urban-induced rainfall anomalies show dependence on the representations of urban canopy and pre-storm environment
- Storm tracking analyses highlight the role of urban canopy in deflecting convective storm cells around the urban-rural interface

Correspondence to:
L. Yang,
yanglong86123@hotmail.com

Citation:
Yang, L., Li, Q., Yuan, H., Niu, Z., & Wang, L. (2021). Impacts of urban canopy on two convective storms with contrasting synoptic conditions over Nanjing, China. *Journal of Geophysical Research: Atmospheres*, *126*, e2020JD034509. https://doi.org/10.1029/2020JD034509

Received 5 JAN 2021
Accepted 28 FEB 2021

Author Contributions:
Conceptualization: Long Yang
Formal analysis: Long Yang, Qi Li
Funding acquisition: Long Yang
Methodology: Long Yang
Project Administration: Long Yang
Validation: Long Yang
Visualization: Long Yang
Writing – original draft: Long Yang
Writing – review & editing: Long Yang, Qi Li, Huiling Yuan, Zhixing Niu, Lachun Wang

Abstract Diverse urban-induced rainfall anomalies highlight the need for improved understanding on extreme rainfall in cities. In this study, we examine urban modification of rainfall over Nanjing, China. Our results are based on climatological analyses of hourly rainfall observations and high-resolution Weather Research and Forecasting model simulations coupled with different urban physics schemes. A gridded dataset of urban canopy parameters (UCPs) was developed to better characterize the geometrical features of downtown Nanjing. Two convective storms were investigated to shed light on the impacts of urban canopy on spatial and temporal rainfall variabilities for storms with contrasting synoptic conditions. We show that the model simulations coupled with the multi-layer urban physics scheme and the gridded UCPs can noticeably reduce biases in surface thermal and dynamic fields, but its performance in rainfall patterns varies with storm events. There is a strong convergence zone over the urban-rural interface induced by building complexes, leading to intensified convection for the storm with strong synoptic conditions but bifurcated moisture fluxes for the storm with weak synoptic conditions. Lagrangian analysis of storm elements further illustrates the role of urban canopy in deflecting storm cells approaching the city for the storm under weak synoptic conditions. The magnitudes of positive rainfall anomalies induced by urban canopy range from 60% to 100% of the storm-total rainfall. Our study highlights the necessity of improved characterization of urban canopy and the perturbed atmospheric boundary layer processes in examining urban convective rainfall.

1. Introduction

Urban modification of rainfall has received considerable attention following the pioneering METROpolitan Meteorological Experiment (METROMEX) in the United States since 1970s (e.g., Changnon et al., 1971; Changnon, 1975). Observational and modeling studies have demonstrated clear signatures of urban impacts on rainfall over a large collection of worldwide cities and mainly point to urban heat island (UHI; e.g., Bornstein & Lin, 2000; Dixon & Mote, 2003; Yang, Smith, et al., 2014; Yang et al., 2014; Yu & Liu, 2015), urban canopy (e.g., Bornstein & LeRoy, 1990; Dou et al., 2015; Miao et al., 2011; Niyogi et al., 2011), and airborne aerosols (e.g., Jin et al., 2005; Liang et al., 2018; Rosenfeld, 2000; Zhong et al., 2017) as the main contributing factors. These factors have been comprehensively reviewed in, among others, Shepherd (2005, 2013).

However, previous studies have identified diverse behaviors of urban-induced rainfall anomalies (i.e., the magnitudes and locations of rainfall changes, see summaries in Liu & Niyogi, 2019). This highlights the complexities of land-atmosphere interactions in urban environments that is closely tied to interacting and intricate factors (Zhang, 2020), for instance, interactions between urban forcing and terrain-induced atmospheric circulations (e.g., lake breeze, mountain-valley circulation) in complex physiographic settings (Freitag et al., 2018; Lin et al., 2011; Yang, Smith, et al., 2014), and/or contrasting synoptic conditions of analyzed storms (Debbage & Shepherd, 2018; Reames & Stensrud, 2018; Yang et al., 2019). Based on five-year observational analyses over Beijing, Dou et al. (2015) found bifurcated winds induced by an urban-barrier induced divergence when the UHI is weak, which leads to storms bypass the urban center and a subsequent rainfall enhancement in the downwind region. This is contrasted with the strong-UHI situations that storms tend to be enhanced over the urban center due to the UHI-induced convergence. The results by Dou et al. (2015), together with some other studies (e.g., Jiang et al., 2020; Wu et al., 2019), highlight the

importance of segmenting storms by synoptic conditions and/or pre-storm environments (e.g., UHI intensity) in urban rainfall studies.

In addition, the geometrical features of urban canopy (e.g., urban area fraction, street widths and orientation, building heights and their spatial distributions, etc.) vary across cities, and their impacts on spatial and temporal rainfall variabilities are still not well understood. For instance, climatological analyses based on radar reflectivity fields show limited evidence of storm splitting over the upwind region of the New York City (Yeung et al., 2015), while the complex seems to be true for Berlin, Germany where storms are either deflected or split by the city (Lorenz et al., 2019). These results echo the findings of three case studies over Atlanta, Georgia by Bornstein and Lin (2000). While the role of cities in bifurcating regional flow is revealed by previous case studies (e.g., Miao et al., 2011; Zhang et al., 2019), additional studies are further needed to understand the impacts of urban canopy on spatial and temporal rainfall variabilities.

Modeling analysis based on the Weather Research and Forecasting (WRF)/Urban modeling system provides a useful utility for examining urban modification of rainfall (Chen et al., 2011; J. K. S. Ching, 2013; Liang et al., 2018). The existing urban physics options in the WRF/Urban modeling system, including the Bulk scheme, the single-layer urban canopy model (UCM), the building effect parameterization (BEP), building energy model (BEM), parametrize urban surface processes with different complexities (see details in, e.g., Chen et al., 2011). The capabilities of different urban parametrizations have been extensively investigated in previous studies (e.g., Barlage et al., 2016; Giovannini et al., 2014; Liao et al., 2014; Salamanca et al., 2018; Sharma et al., 2017; Yang et al., 2015) , most of which specifically focus on space-time dynamics of surface heat fluxes, near-surface temperature and wind fields over cities during clear days. The multi-layer urban physics (e.g., BEP) is mostly recommended in reducing simulation biases of near-surface wind fields and temperature, compared to either the single-layer UCM or the Bulk scheme approach. In addition, the WRF/Urban modeling system with the multi-layer urban parametrizations (BEP or BEM) demonstrates improved performance through incorporating a gridded dataset of urban canopy parameters (UCPs; Carter et al., 2012; He et al., 2019, 2020; Shen et al., 2019; Zhang et al., 2019). The gridded UCPs provide additional information about building heights and their spatial distributions, street widths and orientations, etc., and more realistically represent urban surface heterogeneities in the modeling system. For instance, Salamanca et al. (2011) show that the multi-layer urban parametrization (BEP) coupled with gridded UCPs is superior to simulate air temperature than other urban physics schemes in the WRF/Urban modeling system. However, few studies have investigated the capabilities of different urban parametrizations (especially the multi-layer urban parametrization) and the gridded dataset of UCPs in rainfall simulation using the WRF/Urban modeling system (Li et al., 2013; Miao et al., 2011; Paul et al., 2018; Ryu et al., 2015; Yang, Smith, et al., 2014; Yu & Liu, 2015). Better understandings of the contrasting simulated rainfall fields with different urban parametrizations and geometrical representations of urban canopy can further shed light on the signatures of urban impacts on rainfall. This is of paramount importance due to the strong sensitivities of spatial and temporal rainfall variabilities to different urban representations (e.g., Li et al., 2013; Ryu et al., 2015; Yang, Smith, et al., 2014).

In this study, we focus on two convective rainfall events, that is, the 10 June 2017 storm and 30 June 2018 storm, over Nanjing, the capital city of Jiangsu province in eastern China. Both storms produced extreme short-term rainfall, but with contrasting spatial-temporal rainfall variabilities and pre-storm environments (see details in Section 3). Comparisons between the two storms will further underscore the dependence on synoptic conditions (e.g., Jiang et al., 2020; McLeod et al., 2017; Wu et al., 2019; Yang et al., 2019; Zhang, 2020) in shaping the urban signatures of extreme rainfall. We also expect to provide improved understandings of the impacts of urban canopy on rainfall variabilities. This is mainly because less consensus has been reached on the specific role of urban canopy in dictating rainfall anomalies over cities compared to the overall understandings of urban thermal influences.

The city of Nanjing is an ideal setting for urban rainfall modification studies. It is located in the Yangtze River Delta region, one of the largest urban agglomerations in the world. There are no complex terrain or land-water boundaries (e.g., lake or sea) close to the city. Extreme rainfall over Nanjing is associated with multiple synoptic agents, for example, frontal systems during the East Asian Summer Monsoon period, extra-tropical cyclones, landfalling tropical cyclones, and local convective systems (e.g., Ding & Zhang, 2009). In this study, we first investigate the urban signatures of rainfall anomalies over Nanjing based on climatological

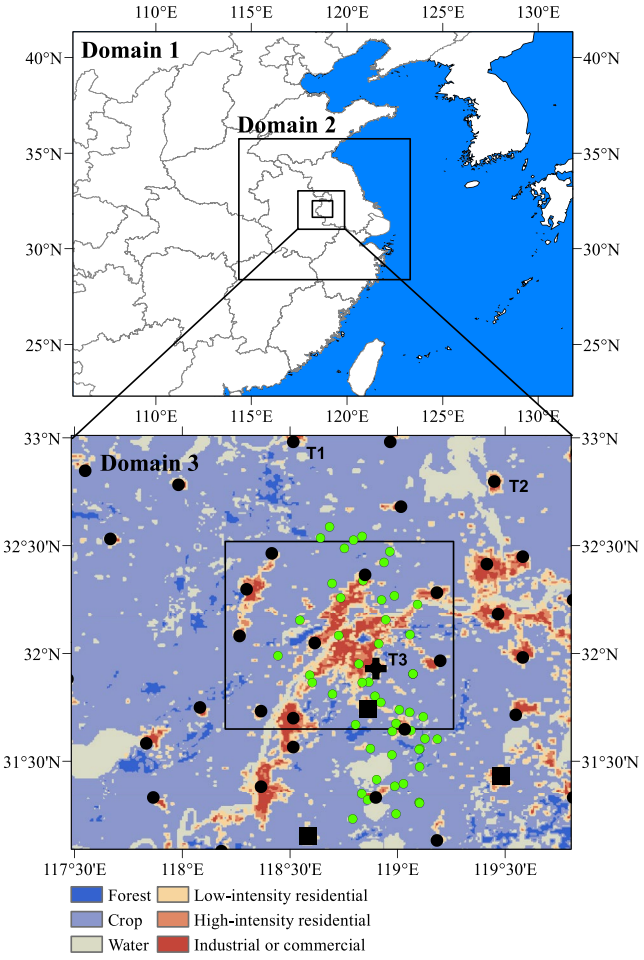

Figure 1. Map of the study region. Three nested domains are outlined in the upper panel. The black box in domain 3 (lower panel) shows the urban domain. Land use/land cover types within domain 3 are shaded. Green dots represent the 42 rain gauges that have complete hourly rainfall records during the period 2013–2017, while black dots show the 29 rain gauges with records of 2018 missing. Black squares and cross represent the 2-m temperature and sounding stations, respectively. The labels (e.g., T1, T2, T3) indicate the locations of three stations with observed daily mean temperature at 2 m.

analysis of hourly rainfall observations. We further focus on the impacts of urban canopy on spatial and temporal rainfall variabilities based on the WRF/Urban modeling system with different urban parametrizations (i.e., the bulk scheme, UCM, and BEP) and improved geometrical representations of urban canopy by incorporating a newly developed dataset of UCPs. The gridded UCPs have been developed for selected cities in the United States through the National Urban Database and Access Portal Tool (NUDPAT, e.g., Ching et al., 2009), but are available only for Beijing and Guangzhou in China (He et al., 2019; Shen et al., 2019).

Our empirical and modeling analyses are centered on the following research questions: (1) What are the urban signatures in the spatial variability of extreme rainfall over Nanjing? (2) What are the utilities of the WRF/Urban modeling system with different urban parametrizations and different geometrical representations of urban canopy in capturing dynamic and thermal fields over cities? (3) What are the impacts of urban canopy on spatial and temporal rainfall variabilities for storms with contrasting pre-storm environments? (4) How do storm structures and evolution properties behave in response to different urban forcing (i.e., perturbations of building complexes and their spatial configurations)?

2. Data and Methodology

2.1. Observations

There are 71 rain gauges with hourly rainfall observations during the warm-season months (i.e., May to September) of 2013–2018 over and around Nanjing (see the lower panel of Figure 1 for locations of the gauges). The dataset is jointly collected from the China Meteorological Administration (29 gauges) and the Hydrological Bureau of Jiangsu province (42 gauges) and is quality controlled for accuracy and consistency throughout the observational period. The 29 CMA gauges do not have records during the entire warm season of 2018 (see Figure 1 for locations) and will be discarded for climatological analyses (see Section 3). There are three meteorological stations that provide 3-h surface air temperature at 2 m (see the lower panel of Figure 1 for locations) during the period of two storm events. There are three additional meteorological stations with daily mean temperature during the period of two storm events. Surface meteorological observations are also obtained from the China Meteorological Administration. We also obtain vertical wind profiles from a sounding station located in the city of Nanjing. The sounding observations are provided by the Integrated Global Radiosonde Archive (IGRA) and are available twice a day (i.e., 00 UTC and 12 UTC) during the two storms (see the lower panel of Figure 1 for its location). These in situ observations mainly serve the purpose of model evaluation, except that analyses of rain gauge observations highlight the spatial variability of warm-season extreme rainfall over Nanjing from a climatological perspective.

2.2. Gridded Data

We develop a high-resolution gridded dataset of UCPs to better characterize the geometrical features of urban canopy over Nanjing. The gridded UCPs are based on a vector-format archive of urban buildings for a collection of major cities in China. The data archive is maintained by the Resources and Environmental Science Data Center of the Chinese Academy of Sciences (see http://www.resdc.cn for details) and provides geometric information of buildings over the downtown area, including building profile, height, and their locations. The dataset of updated UCPs includes the following variables: the mean, standard deviation, and

Table 1
Overview of WRF Physics Options

	Domain 1	Domain 2	Domain 3
No. of horizontal grid cells (x, y)	200 × 200	271 × 268	229 × 226
Grid size (km)	9	3	1
Time steps (s)	54	18	6
Cumulus scheme	K-F scheme	None	None
Microphysics scheme	WSM6		
Vertical layers	38 levels, with 15 levels below 2 km		
Long wave radiation	RRTM Scheme		
Short wave radiation	Dudhia Scheme		
Surface layer	Monin-Obukhov Scheme		
Land surface	Noah Land Surface Model		
Boundary layer	Mellor-Yamada-Janjic (MYJ) scheme		
Land use Initial and Boundary Conditions	MODIS 30s, with updated urban land use categories based on 30-m impervious coverage over China (see Liu et al., 2018)		
	NCEP FNL analysis fields (6 h, 1°)		

histogram of building height, building plan area fraction, building surface area to plan area ratio, frontal area indexes for northerly, north-easterly, easterly, and south-easterly winds. The other information, such as roof/street width, building width, sky-view factor, etc., can be calculated accordingly. The list of gridded UCPs is shown in Table 2. The readers are referred to Burian and Ching (2009) for detailed procedures about the development of gridded UCPs.

The urban land-use/land-cover over Nanjing is updated based on a 30-m impervious cover map developed by Liu et al. (2018) (see http://www.geosimulation.cn/GlobalUrbanLand.html for details). The urban land use was classified into three sub-categories according to the percentage of total impervious coverage (IR) within a 1-km^2 grid, that is, low-intensity residential (IR < 0.5), high-residential (0.5 < IR < 0.8), and commercial/industrial (IR > 0.8, similarly, see, e.g., Yang, Tian, et al., 2014). The percentage of total impervious coverage within a 1-km^2 grid is also termed as urban fraction. Urban fraction controls the partition of surface fluxes between the vegetated and non-vegetated portion within an urban grid and is a critical variable in dictating the radiative fluxes and surface meteorological fields in the WRF/Urban modeling system (e.g., Chen et al., 2011; Li et al., 2013). The gridded UCPs are incorporated into the WRF/Urban modeling system to better characterize the geometrical features of urban canopy over Nanjing.

2.3. WRF Modeling

We use the WRF model to examine two storm events, that is, the 10 June 2017 storm and 30 June 2018 storm. The WRF model is a fully comprehensible, non-hydrostatic, mesoscale model (Skamarock et al., 2019). The version of Advanced Research WRF V4.0 was used. We set up three two-way nested domains (Figure 1), with the outer domain (domain 1) covering central and south-eastern China and the innermost domain centering over Nanjing. There are 200 × 200, 217 × 268, and 229 × 226 horizontal grids, with grid spacings of 9, 3, and 1 km for the three domains, respectively. We configured 38 vertical levels in the model, with 15 of them below 2 km above the ground, to better capture dynamical processes within atmospheric boundary layer. The upper boundary of the model is set at 100 hPa. The physics options used in the simulations include: the WRF single-moment six-class (WSM6) microphysics scheme, the Mellor-Yamada-Janjic (MYJ) boundary layer scheme, the Rapid Radiative Transfer Model (RRTM) for long-wave radiation, Dudhia's scheme for short-wave radiation, and the Noah land surface model. The Kain-Fritsch cumulus scheme is only adopted for the outer domain. Details of main physics options of the WRF simulations are summarized in Table 1.

Table 2
List of Gridded UCPs and Default UCM/BEP Parameters Adopted in WRF Simulations

Name of	Default UCM/BEP parameters			
Gridded UCPs	Name (unit)	Low-intensity residential	High-intensity residential	Commercial/industrial
HGT_URB2D	BUILD_HEIGHT (m)	5.0	7.5	10.0
LP_URB2D	BUILD_AREA_FRACTION (−)	No	No	No
LB_URB2D	BUILD_SURF_RATIO (−)	No	No	No
FRC_URB2D	FRC_URB (−)	0.50	0.90	0.95
BW_URB2D	ROOF_WIDTH (m)	8.3	9.4	10.0
SW_URB2D	ROAD_WIDTH (m)	8.3	9.4	10.0
ZDC_URB2D	ZDC (m)	1/5 of ZR	1/5 of ZR	1/5 of ZR
Z0C_URB2D	Z0C (m)	1/10 of ZR	1/10 of ZR	1/10 of ZR
Z0HC_URB2D	Z0HC (m)	1/10 of Z0C	1/10 of Z0C	1/10 of Z0C
Z0R_URB2D	Z0R (m)	0.01	0.01	0.01
HI_URB2D	Height_bin	5 m (15%)	10 m (20%)	15 m (10%)
	Height/(Percentage)	10 m (70%)	15 m (60%)	20 m (25%)
		15 m (15%)	20 m (20%)	25 m (40%)
				30 m (25%)

Notes. The definitions of listed parameters are as follows. HGT_URB2D: area weighted mean building height, LP_URB2D: building plan area fraction, LB_URB2D: building surface to plan area fraction, FRC_URB2D: fraction of non-vegetation surface, BW_URB2D: roof width, SW_URB2D: road width, ZDC_URB2D: zero plane displacement height, Z0C_URB2D: roughness length for momentum above canyon, Z0HC_URB2D: roughness length for heat above canyon, Z0R_URB2D: roughness length for momentum above roof, HI_URB2D: building height bins defined for a particular urban category.

We implement five different numerical simulations for each of the two storm events. The aforementioned model configurations are used for each set of the five simulations scenarios. Details of different simulation scenarios are summarized in Table 3. The simulations differ from each other by contrasting urban physics schemes and/or UCPs only. The UCM_TAB and UCM_UCP simulations describe the interactions of urban surface and lower atmosphere through coupling a single-layer UCM to the Noah land surface model, while the multi-layer building effect parametrization (BEP) is adopted in the BEP_TAB and BEP_UCP simulations. Unlike the single-layer UCM that categorizes urban surfaces into roofs, roads, and walls, the BEP model additionally resolves the effects of urban buildings on heat and momentum transport throughout the urban canopies (defined by the depth from the ground surface to the height of the tallest buildings within the domain). The effects can propagate into the regions above the urban boundary layer through the transport processes as prescribed by the prognostic equations within the WRF/Urban modeling system. The BULK simulation uses a simple urban treatment (i.e., the bulk roughness approach) in the default Noah land surface model and does not consider the spatial heterogeneity of urban surface properties.

Table 3
Overview of Different Simulation Scenarios

Scenarios	Urban physics	Urban canopy parameters
BULK	Bulk scheme approach	None
UCM_TAB	Single-layer urban canopy model	Look-up table
UCM_UCP	Single-layer urban canopy model	Gridded UCPs
BEP_TAB	Multi-layer building effect parametrization	Look-up table
BEP_UCP	Multi-layer building effect parametrization	Gridded UCPs

Note. See the text for details about each scenario

The gridded dataset of UCPs developed in Section 2.2 is incorporated in the UCM_UCP and BEP_UCP simulations. This is contrasted with the UCM_TAB and BEP_TAB simulations that adopt default UCPs from a look-up table (Table 2, see more details in Chen et al., 2011). We provide a quantitative comparison between the key geometrical features of urban canopy over Nanjing characterized by the default look-up table and by UCPs (Table 4). Figure 2 additionally show selected variables of UCPs over Nanjing. The urban fraction field spans from 0 to 1 over the entire city, with the mean value of 0.62. This is contrasted with a larger mean urban fraction value (i.e., 0.77) based on the default look-up table. The mean building height in UCPs is 14.4 m, with the maximum value of 68.1 m, while the mean and maximum values are 7.4 and 10.0 m, respectively based on the default look-up table. The mean values of roof/street widths are comparable between UCPs and the default look-up

Table 4
Statistics of Urban Buildings Over Nanjing as Prescribed by the Default Look-up Table and UCPs

	Building height (m)		Urban fraction (−)		Roof/street (m)	
	Table	UCPs	Table	UCPs	Table	UCPs
Mean	7.4	14.4	0.77	0.62	9.4	10.2
Standard deviation	2.0	9.2	0.21	0.24	0.71	5.9
Minimum	5.0	3.0	0.5	0.06	8.3	1.5
Maximum	10.0	68.1	0.95	1.0	10.0	100.7

table, although the roof/street widths in UCPs show relatively larger spatial variabilities. Comparisons of building height and urban fraction indicate that higher but less dense urban buildings are characterized by UCPs than the default look-up table. An interesting finding is that there are several "hot-spots" of high buildings distributed over the outer boundary of downtown Nanjing (Figure 2b). This spatial pattern of building heights is tied to the local land policy that historical buildings need to be well preserved within the city, while numerous high-rise residential buildings are constructed outside downtown to accommodate increasing city dwellers. This is clearly different from the spatial pattern of building heights as characterized by the default look-up table that the highest buildings are distributed over downtown (i.e., consistent with the distribution of commercial/industrial urban category, see Figure 1).

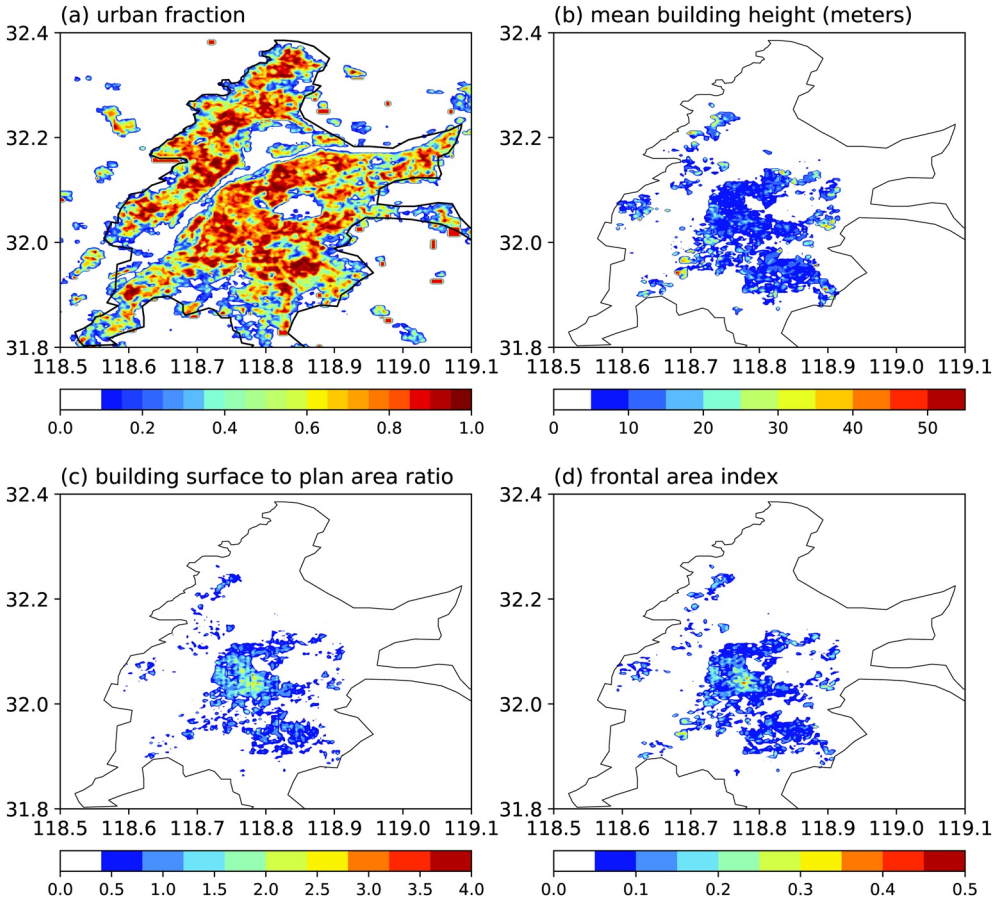

Figure 2. Spatial map of selected variables in the gridded urban dataset for Nanjing: (a) urban fraction (−), (b) mean building height (in meters), (c) building surface to plan area ratio (−), and (d) frontal area index (−) in south direction. The black line shows the urban boundary of Nanjing.

In addition to the aforementioned contrasts in how urban surfaces are parametrized, the representations of anthropogenic heat are different among three urban parameterizations (i.e., the bulk scheme, UCM, and BEP). There is no consideration of anthropogenic heat in the bulk scheme. A default diurnal profile of anthropogenic sensible heat is adopted for the single-layer UCM (e.g., Chen et al., 2011), while the multi-layer BEP can be incorporated with BEM to explicitly represent anthropogenic sensible and latent heat fluxes released from urban buildings (e.g., Gutiérrez et al., 2015; Salamanca et al., 2011). Anthropogenic heat can influence spatial and temporal distributions of urban rainfall through modifying thermodynamic fields over cities (Nie et al., 2017). In this study, we turned off anthropogenic heat for each simulation scenario. This enables that comparisons among different simulations can be attributed to only urban parametrization itself and how the geometrical features of urban canopy are characterized. The deviations of simulations from observations can be partially resulted from the absence of anthropogenic heat, but are quite limited (see model evaluation in Section 4.1).

The simulations for the 10 June 2017 storm are initiated at 00 universal time coordinated (UTC) on 09 June 2017, and run for 48 h. The simulations for the 30 June 2018 storm are initiated at 00 UTC on 30 June 2018 and run for 48 h. The first 6-h period for each set of the simulations is treated as model spin-up period and not included in the following analyses. We principally focus on the innermost domain (i.e., domain 3) due to its highest grid resolution and its ability to capture the small-scale convective activities. The temporal interval of the output is 1 h for the innermost domain. The initial and boundary conditions for the WRF simulations are provided by the meteorological fields obtained from the National Centers for Environmental Prediction (NCEP), Final (FNL), and Global Forecast System (GFS) analyses. The GFS FNL reanalysis fields, with the spatial resolution of 1° and temporal resolution of 6 h, are also used to characterize the synoptic conditions for the two storms.

2.4. Storm Tracking

We perform Lagrangian analyses for the simulated 30 June 2018 storm event using the Thunderstorm Identification, Tracking, Analysis, and Nowcasting (TITAN) storm tracking algorithms (Dixon & Wiener, 1993). We create reflectivity fields for each of the five WRF simulations based on the simulated hydrometeor fields and convert them to 3-D Cartesian fields. The vertical and horizontal resolution of the reflectivity fields is 1 km. The storm tracking analyses are based on model simulations with a temporal interval of 10 min, and span the dominant rainfall period 1000 UTC–1600 UTC on 30 June 2018. We use a 45 dBZ reflectivity threshold and a 5 km^3 volume threshold to identify storm elements for the 30 June 2018 storm. A storm cell is identified as a contiguous region of reflectivity values exceeding 45 dBZ provided that the total volume of the contiguous region is greater than 5 km^3 (similarly see, e.g., Ryu et al., 2015; Yang & Smith, 2018; Yang, Smith, et al., 2014, 2016). Results based on a different set of thresholds (i.e., 40 dBZ and 30 km^3) do not show considerable differences (results not shown). The 2018 storm is chosen for tracking analyses particularly due to that extreme rainfall over the city is closely associated with a single complex storm track and its temporal evolution property. The role of urban canopy can be easily interpreted based on differences among the simulated storm tracks. This contrasts with the 2017 storm that multiple complex storm tracks are responsible for extreme rainfall and make the storm tracking results unable to be directly related to urban effects (results not shown).

3. Extreme Urban Rainfall

3.1. Rainfall Climatology

Figure 3 shows the spatial distributions of extreme rainfall statistics based on 71 gauges of hourly rainfall observations during the warm seasons of 2013–2017 over Nanjing. We use the 99th percentile hourly rain rate for each rain gauge (in Figure 3a) as the threshold for extreme short-term rainfall. There are three gauges with the thresholds exceeding 28 mm/h and are located over the city, with several others nearby exceeding 25 mm/h on average. The hourly rain rates decrease to 17 mm/h over the surrounding rural areas. There is a pocket of rain gauges with the rain rates averaging around two thirds of the maximum to the south of downtown Nanjing (Figure 3a). Consistent with the spatial pattern of extreme hourly rain rates, the gauges with the largest 99th percentile hourly rain rates also show the most frequent hours with rain

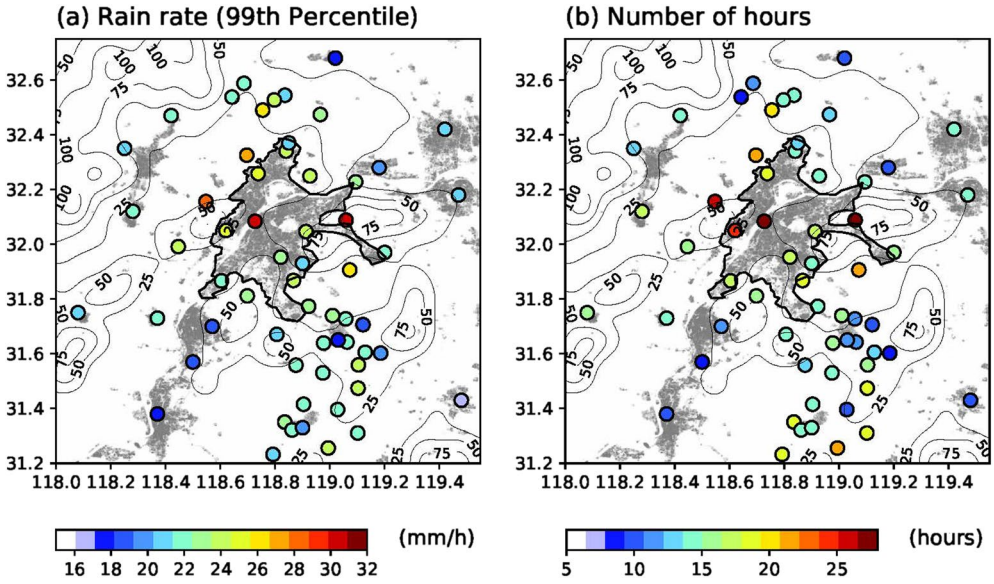

Figure 3. Spatial distributions of (a) the 99th percentile hourly rain rate and (b) number of hours with rain rates exceeding 20 mm/h. Results are based on five-year hourly rainfall observations during the warm seasons of 2013–2107. Gray shading highlights impervious coverage. The black line shows the urban boundary of Nanjing. The contours represent terrain (in m).

rates exceeding 20 mm/h (i.e., around 28 h, see Figure 3b). The total number of extreme rainfall hours (i.e., exceeding 20 mm/h) sharply decreases to 7.5 h on average (i.e., 3–4 times smaller than the peak) within approximately 50 km away from downtown Nanjing. We show a strong urban signature in dictating spatial rainfall variability over Nanjing as reflected by the concentrations of extreme hourly rain rates and their frequencies over the city. An important caveat is that the revealed urban signature is based on climatological analyses which mix all storm events regardless of their pre-storm environments. The following analyses for two representative storm events will be carried out to further investigate the urban signature in characterizing rainfall anomalies over Nanjing.

3.2. Synoptic Overviews

The two events examined in this study are the 10 June 2017 storm and the 30 June 2018 storm. Both storms are short-term convective rainfall events during the East Asian Summer Monsoon period (i.e., June to August; Ding & Chan, 2005; Ding & Zhang, 2009). However, the two storms show contrasting synoptic conditions, spatial and temporal rainfall variabilities, and the resultant socio-economic impacts. For reasonable comparisons, we count on 42 rain gauges that have records during both storm events, most of which are located within the urban domain (see Figure 1 for locations). There are 30 (5) gauges with peak hourly rain rates exceeding 20 mm/h (40 mm/h) for the 10 June 2017 storm, with the maximum value of peak hourly rain rates around 56 mm/h, while there are only 7 (1) gauges with peak hourly rain rates exceeding 20 mm/h (40 mm/h) for the 30 June 2018 storm, with the maximum value of peak hourly rain rates around 45 mm/h. The maximum 24-h rainfall accumulation is 244 mm for the 10 June 2017 storm, with a return interval of more than 100 years. Additional 4 gauges with daily rainfall accumulation exceed 200 mm, and set new records since the establishment of the gauges in Nanjing. The 10 June 2017 storm passed through Nanjing during a 12-h period, that is, from 1600 UTC on 9 June 2017 to 0400 UTC on 10 June 2017. This late-night-early-morning storm resulted in severe inundation for 16 locations and paralyzed the transportation system over downtown Nanjing. In contrast, the 30 June 2018 storm is a fast-moving event, with limited spatial and temporal coverages. The peak rainfall mainly concentrated in 1–2 h for most rain gauges. The daily rainfall totals for the 30 June 2018 storm are less than 50 mm for all the 42 rain gauges, with a maximum value around 47 mm. Unlike the 30 June 2017 storm, there are limited consequences in terms of flood inundation or socio-economic losses for the 30 June 2018 storm.

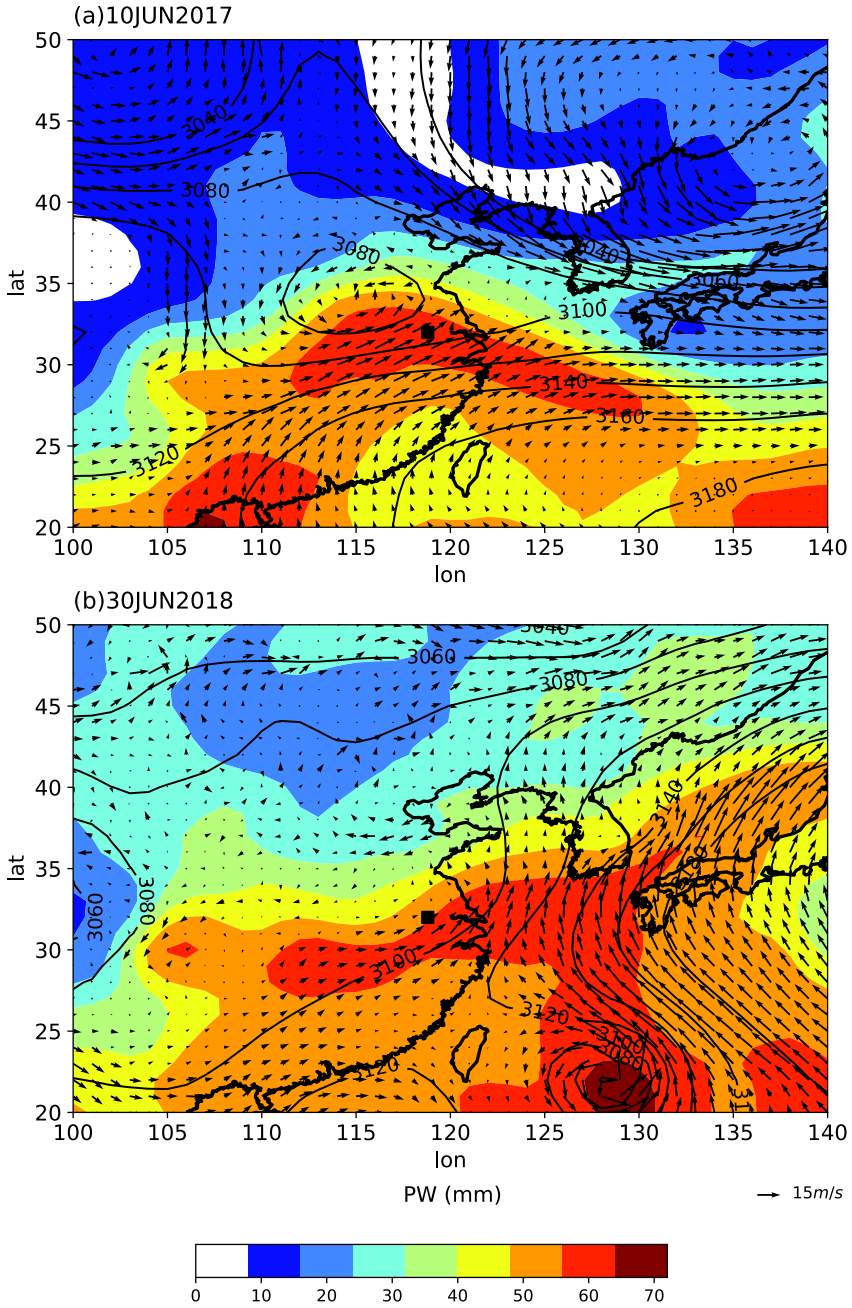

Figure 4. Pre-storm environment for the (a) 10 June 2017 (at 1800 UTC) and (b) 30 June 2018 storm (at 0600 UTC). Black contours represent geopotential height (in gpm) at 700 hPa, while shading represents precipitable water integrated within the entire air column (in mm). Vectors show wind fields at 700 hPa. Black square shows the location of Nanjing. The thin black lines outline coastal boundaries. The results are based on GFS FNL fields.

Contrasting spatial and temporal rainfall variabilities are closely associated with different synoptic conditions for the two storms. The 10 June 2017 storm is associated with the passage of an extratropical cyclone over the middle reaches of the Yangtze River and Huai River basins (also frequently known as Jianghuai Cyclone, see, e.g., Chang et al., 1998; Ding & Zhang, 2009). The Jianghuai Cyclone is a typical synoptic system responsible for extreme rainfall and widespread flooding in the lower portion of the Yangtze River basin (Chang et al., 1998). The closed contour of 3080 gpm at 700 hPa formed at 1800 UTC, and gradually swept across the lower reach of the Yangtze River basin (Figure 4a). The maximum wind speed exceeded 20 m/s and transported tremendous amount of moisture from the tropics to the storm region. The wind direction

at the steering-level is from south-west toward north-east. Extreme rainfall was mainly concentrated in the warm-sector of the cyclone. The precipitable water throughout the entire air column is around 70 mm before the storm.

In contrast, the synoptic condition for the 30 June 2018 storm is relatively benign (Figure 4b). The storm propagated from north of the city toward the city center. The air-column integrated precipitable water is approximately 55 mm. The convective available potential energy at 0600 UTC (1400 LST, i.e., LST = UTC+8h) is over 1300 J/kg for the 30 June 2018 storm, indicating a strong potential for convection before the storm. Based on visual checking on the radar loops of composite reflectivity fields, the 30 June 2018 storm is characterized by scattered convective storm cells that are not well organized in space, while the 10 June 2017 storm shows storm structure of a mesoscale convective system. This type of storm development for the 30 June 2018 storm can be related to surface heating in early afternoon and the pre-existing moist convective energy accumulated in the atmosphere. In addition to the aforementioned contrasts in synoptic conditions, the thermal contrasts between urban and rural areas, that is, the UHI intensity, are different between the two storms. The UHI intensity is defined as the 2-m air temperature difference between the urban station (i.e., the station located in the black box in Figure 1) and the average of the two rural stations for during the 6-h period before the initiation of the storms (i.e., 1800 UTC 09 June 2017 and 12 UTC 30 June 2018, respectively). The UHI intensity is around 1.1 °C for the 2017 storm, and is 0.6 °C for the 2018 storm.

4. WRF Results

4.1. Thermal and Dynamic Fields

Figure 5 shows the spatial patterns of daily mean temperature for the 10 June 2017 and 2030 June 2018 storm. All the five simulations capture key features of surface temperature pattern for both storms. For instance, there is a strong spatial gradient of surface temperature from north to south for the 2017 storm (Figure 5). The simulated patterns of surface temperature are comparable among the simulations, although the BULK simulation seems to produce the largest temperature biases over the urban region. We further evaluate our simulations at the locations of the three in-situ meteorological stations and the corresponding model grids for both storm events, with the statistics summarized in Table 5. The statistics are combined for both storm events, since the two events do not show noticeable differences in terms of the statistics. There are 84 sample hours for each statistic. As can be seen from Table 5, all the five simulations reasonably capture the spatial and temporal variabilities of surface air temperature, with the mean bias around 1 °C and the correlation coefficient around 0.95 for the urban station. Compared to the BULK simulation, the simulations using either the single-layer UCM or BEP reduce the mean biases of 2-m temperature, with the two BEP simulations (i.e., BEP_TAB and BEP_UCP) demonstrating better performance than the two UCM simulations (i.e., UCM_TAB and UCM_UCP). In addition, incorporating the upgraded UCPs in the BEP_UCP simulation further shows improvement in capturing the temporal variability of 2-m temperature over the three stations (see correlation coefficient statistics in Table 5). For instance, the mean bias for the urban station (i.e., the one located within the urban domain) is 1.11 °C in BEP_TAB and is reduced by about 0.1 °C in BEP_UCP. Both the statistics of RMSE and correlation coefficient are improved in the BEP_UCP simulations for the urban station. The utility of gridded UCPs has also been examined in Carter et al. (2012) and Gutierrez et al. (2011). Shen et al. (2019) and He et al. (2019) also highlight the utility of the WRF model with multi-layer urban physics and upgraded UCPs in improving thermodynamics over urban surfaces during clear days. Our simulation results further show that the benefits of incorporating gridded UCPs are still noticeable during rainfall periods.

There are noticeable contrasts in 2-m temperature averaged over all urban grids (i.e., with the land use type categorized as low-intensity residential, high-residential, or commercial/industrial) among the simulations for both storm events. The maximum and mean 2-m temperature for the two BEP simulations for both storm events is about 2 °C lower than the BULK simulation, and 1 °C lower than the two UCM simulations (Figures 6a and 6b), respectively (see also Figure 5 for spatial patterns). Contrasts in surface temperature are partially tied to surface energy partitioning over urban surfaces (e.g., Yang, Smith, et al., 2014; Yang, Wang, et al., 2016). The mean values of latent heat flux, that is, about 100 W m^{-2}, for the UCM_UCP and BEP_UCP simulations are comparable, but are much larger than the other three simulations (i.e., with the median values of about 10 W m^{-2}, Figures 6c and 6d). The contrary is true for sensible heat fluxes (Figures 6e and 6f).

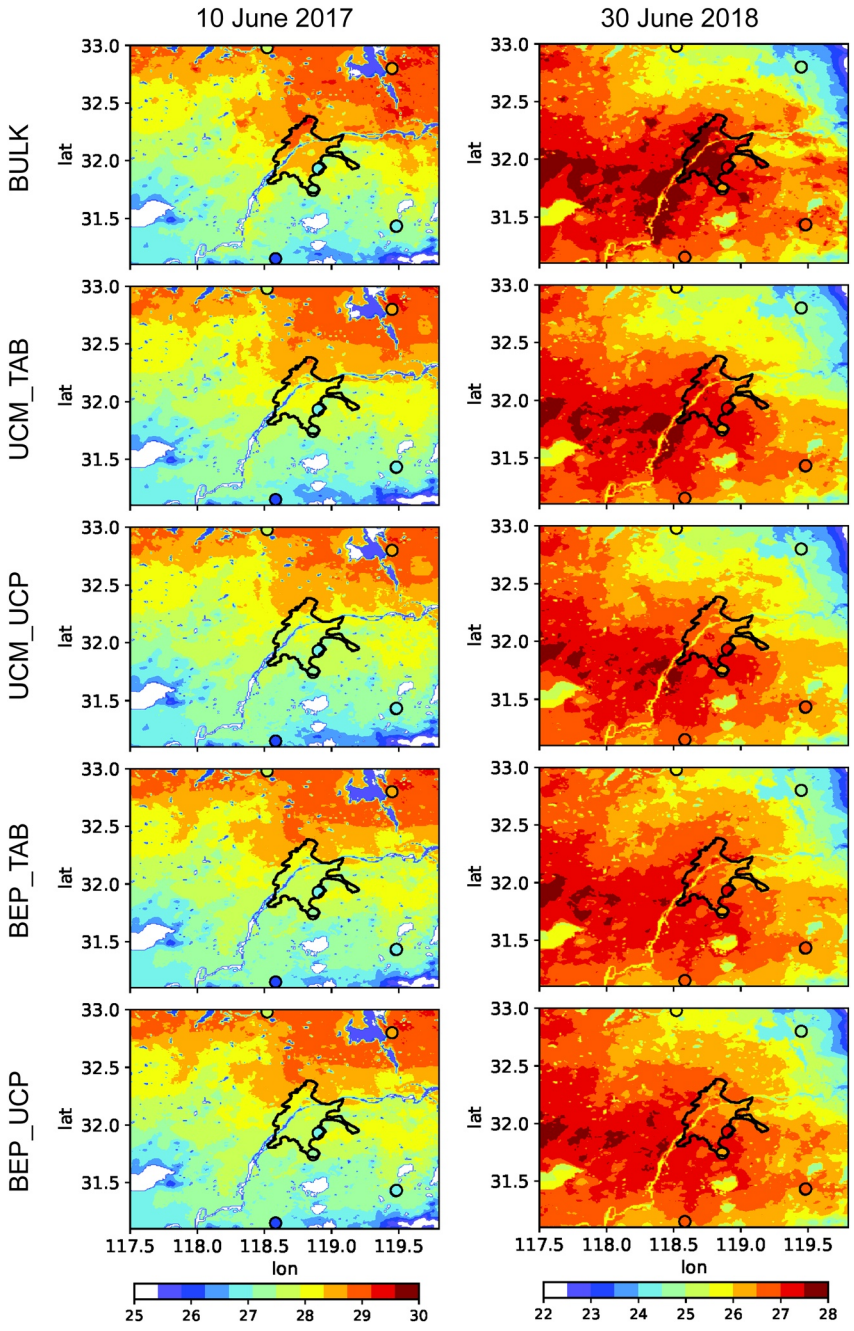

Figure 5. Spatial patterns of simulated daily mean 2-m temperature for 09 June 2017 (left panel) and 30 June 2018 (right panel). Dots in the map represent temperature observations from six meteorological stations. Black line shows the urban boundary of Nanjing.

The overestimation (underestimation) for sensible (latent) heat flux in the BULK simulation is due to configurations in the Noah land surface model with the non-vegetation cover taking up the entire urban grid (i.e., urban fraction equal to 1). The mean urban fraction characterized by UCPs is much smaller than that by the default look-up table (Table 4), indicating less impervious coverage for a urban grid in the UCM_UCP and BEP_UCP simulations that promotes more latent heat flux contributed from evapotranspiration over the vegetated portion (e.g., Salamanca et al., 2018; Templeton et al., 2018; Vahmani & Hogue, 2014). This echoes the lower 2-m temperature in the two BEP simulations compared to the BULK simulation and leads to slightly larger urban-rural thermal contrasts in the BULK simulation than the two UCM and BEP

Table 5
Statistics of 2-m Temperature Between Meteorological Stations and the Corresponding Model Grids for Both Storm Events

	Mean bias (°C)			RMSE (°C)			Correlation coeff.		
	Station 1	Station 2	Station 3	Station 1	Station 2	Station 3	Station 1	Station 2	Station 3
BULK	1.19	1.74	1.06	1.47	2.05	1.42	0.95	0.89	0.94
UCM_TAB	1.13	1.69	0.93	1.46	1.96	1.30	0.94	0.87	0.96
UCM_UCP	1.11	1.57	1.36	1.30	1.96	1.73	0.95	0.86	0.93
BEP_TAB	1.11	1.45	1.09	1.40	1.75	1.31	0.94	0.88	0.93
BEP_UCP	1.02	1.44	1.03	1.29	1.74	1.24	0.95	0.87	0.95

Notes. "Station 1" represents the station located within the black box shown in the lower panel of Figure 1. See the texts for details about each scenario.

simulations. Differences between urban parametrizations, that is, single-layer or multi-layer, seem to have played a smaller role in determining surface energy fluxes over the entire city (Figure 5).

Figure 7 compares vertical wind profiles between the sounding observation and WRF simulations. The two BEP simulations capture key features of vertical wind profiles for both storm events, while the BULK simulation and the two UCM simulations overestimate wind speeds for almost all vertical levels compared to the sounding observations especially for the 10 June 2017 storm (Figure 7a). The sounding profile shown in Figure 7 provides additional insights into the pre-storm environment for the 10 June 2017 storm. There is a local maximum of wind speeds (i.e., exceeding 12 m/s) around the level of 950 hPa, indicating the existence of a low-level jet. A consistent feature is that all the five simulations show peak wind speeds around 50 hPa above the ground. The low-level jet, through transporting a moist, unstable plume from the tropics,

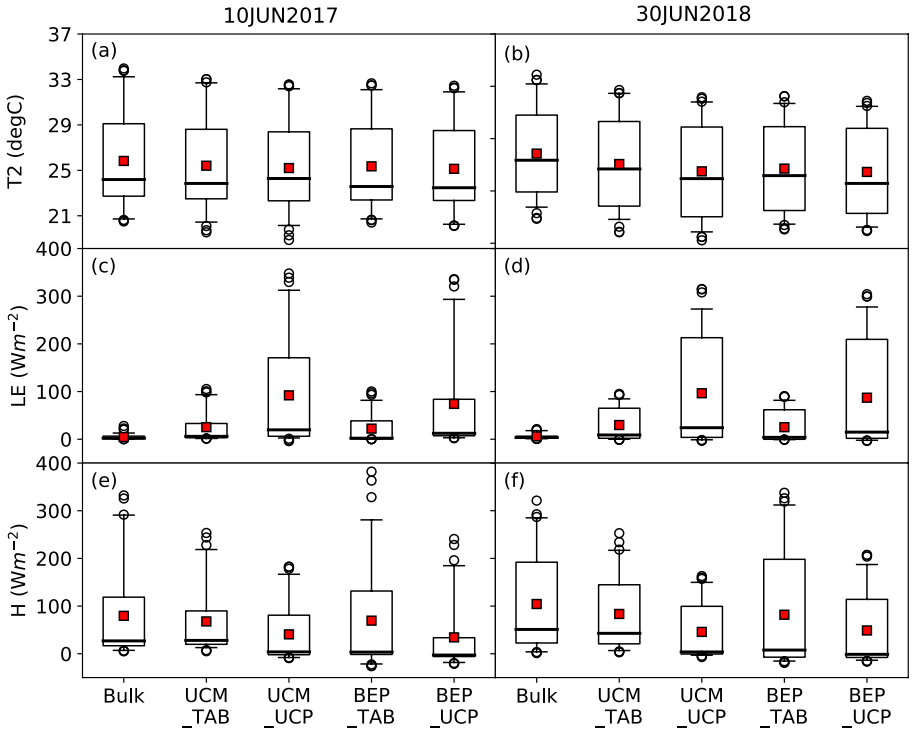

Figure 6. Boxplots of hourly 2-m temperature (in °C, upper panels), latent heat flux (in W m^{-2}, middle panels), and sensible heat flux (in W m^{-2}, lower panels) averaged over the urban domain, for the 10 June 2017 (left panels) and 30 June 2018 storm (right panels). The box spans the 25th and 75th percentiles, and the whiskers represent the 5th and 95th percentiles. The black lines and red squares in the box represent the median and mean values, respectively.

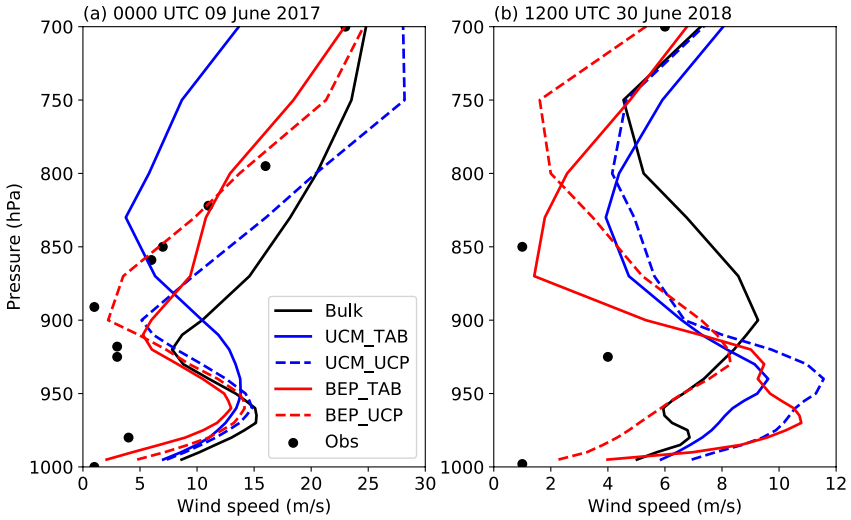

Figure 7. Vertical wind profiles at (a) 0000 UTC on 09 June 2017, and (b) 1200 UTC on 30 June 2018. Black dots represent sounding observations.

is responsible for extreme rainfall in the subsequent hours for the 10 June 2017 storm (see also synoptic overviews in Section 3.2 and Figure 4a). The performance of WRF simulations for the vertical wind profile of the 30 June 2018 storm cannot be adequately evaluated due to sparse data points, although the bias of wind speeds seems to be the smallest at the near-surface level in the BEP_UCP simulation and around 850 hPa in the BEP_TAB simulation (Figure 7b).

We further highlight the contrasts in wind fields across different simulations by focusing on the differences between simulations with the single-layer (i.e., UCM_TAB and UCM_UCP) and multi-layer (i.e., BEP_TAB and BEP_UCP) urban parametrization through referencing against the BULK simulation (see Figures 8 and 9). The four WRF simulations reduce 10-m wind speed, with the two BEP simulations demonstrating a much larger spatial extent and magnitudes of reduction in near-surface wind over the city than the two UCM simulations. The reduction is quite noticeable over the city boundaries. For instance, the 10-m wind speed for the BEP simulations is 7 m/s smaller than the BULK simulation over the northern boundary (i.e., upwind) of the city for the 30 June 2018 storm (Figure 9). The UCM_UCP and BEP_UCP simulations further show reduction in 10-m wind speeds than their counterpart simulations, that is, UCM_TAB and BEP_UCP (figures not shown). The results are expected as surface roughness is increased over the city tied to the relatively larger building heights in UCP simulations (i.e., UCM_UCP and BEP_UCP) than those with the default look-up table (i.e., UCM_TAB and BEP_UCP). However, unlike surface heat fluxes, contrasts in surface wind fields induced by different geometrical representations of urban canopy are less notable than those induced by different urban parametrizations. Similarities and contrasts in thermodynamic and dynamics fields among the simulations have implications for spatial and temporal rainfall variabilities for the two storms and will be analyzed below.

4.2. Space and Temporal Rainfall Variabilities

The rainfall accumulation for the 10 June 2017 storm demonstrates a band-shaped distribution that extends from northwest to southeast direction, with rainfall totals exceeding 120 mm along the band (Figure 10). The five WRF simulations can well capture the band-shaped distribution of accumulated rainfall for the 10 June 2017 storm, but are different in placing the storm bands relative to the city. Only the two BEP simulations place the storm bands across the city, with the BEP_TAB simulation more specifically producing a comparable coverage of extreme rainfall (e.g., more than 175 mm) to rain gauge observations over the southern portion of the city (Figure 10d). The peak rainfall totals, more than 220 mm, from the BEP_UCP simulation are also comparable to rain gauge observations, but show a larger spatial coverage outside the city. Gauge-based statistics of the model evaluation show that the two BEP simulations stand out in capturing spatial rainfall variability for the 10 June 2017 storm, with the BEP_TAB simulation presenting the best

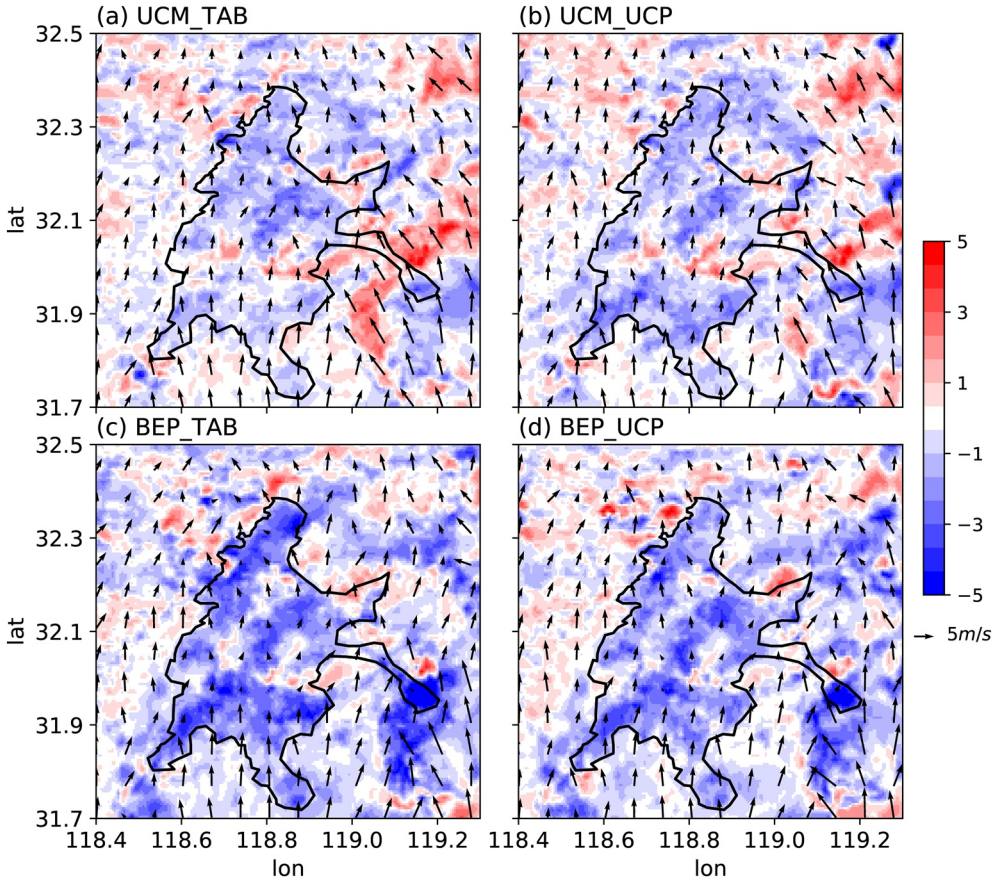

Figure 8. Map for the 10-m wind fields (in m/s) at 0000 UTC for the 10 June 2017 storm. Shading represents differences of 10-m wind magnitude between each simulation scenario and the BULK simulation. Black line shows the urban boundary of Nanjing.

model performance (Table 6 and Figure 10f). This can be possibly attributed to the superior performance of the two BEP simulations in capturing wind dynamics for the 2017 storm (see Figure 7 and Section 4.1), a key ingredient for moisture transport and extreme rainfall for this specific event. The slightly worse of the BEP_UCP simulation than the BEP_TAB simulation is mainly due to the overestimated rainfall outside the city (Figure 10e). This indicates that the multi-layer parameterization incorporated with gridded UCPs produces more noticeable perturbations on rainfall than without gridded UCPs (also see storm tracking analyses in Section 4.4).

It seems to be challenging for the WRF/Urban modeling system to accurately predict the spatial distribution of accumulated rainfall for the 30 June 2018 storm. This is associated with the nature of spatially isolated convective storm cells for this storm. Figure 11 shows strong variations among the five WRF simulations in terms of the location of rainfall extremes and their intensities. Visual checking on the radar loops of composite reflectivity fields further confirms the passage of isolated convective cells across the northern portion of the city. All five simulations show a consistent timing of storm development with the radar loops over the innermost domain, but demonstrate contrasting spatial patterns especially when storm cells approach the city. A notable finding is that rainfall is mainly accumulated along with the urban-rural interface (i.e., in the upwind direction) for the two BEP simulations for the 30 June 2018 storm (Figures 11c and 11d), while observational evidence based on radar loops, intense rainfall is also observed within the city. The observed rainfall peak over the city is tied to the enhanced turbulent mixing within the atmospheric boundary layer induced by surface heating in the late afternoon. The two UCM simulations and the BULK simulation place heavy rainfall over downtown, although rainfall intensities are overestimated compared to gauge observations (Figures 11a–11c). The overestimation of rainfall over the city is tied to the larger urban-rural

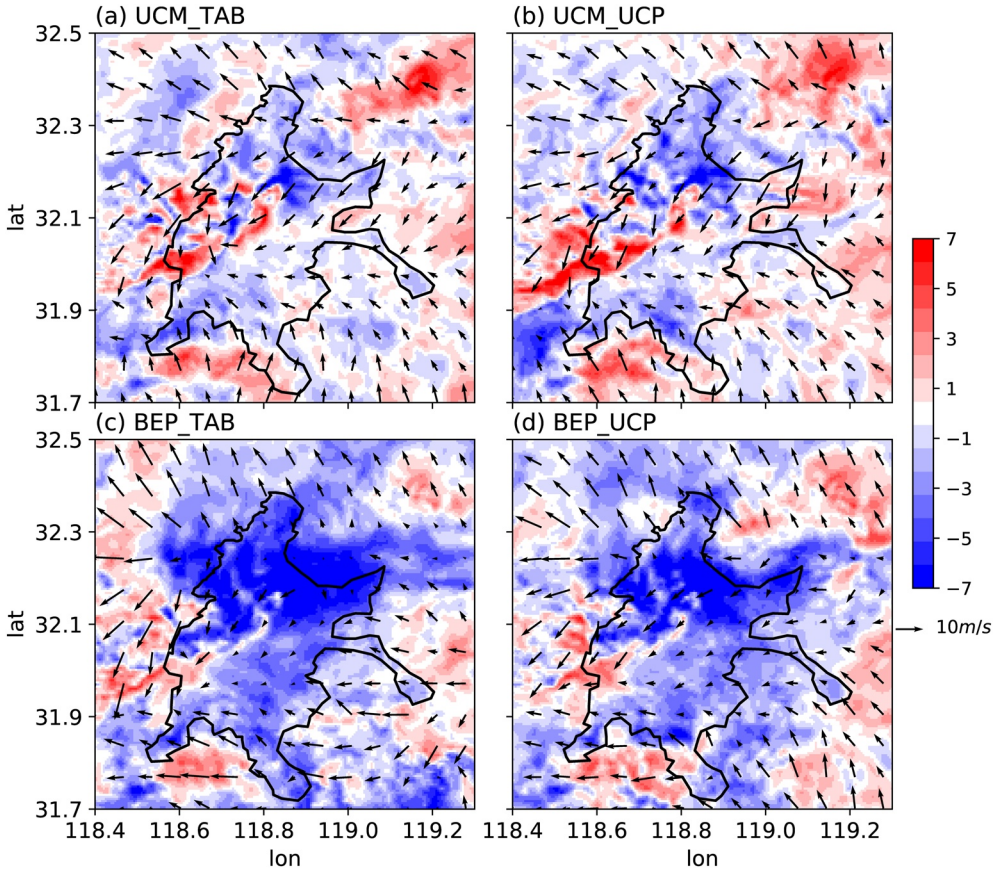

Figure 9. Same as Figure 8, but for the 30 June 2018 storm at 1200 UTC.

thermal contrast shown in the BULK and two UCM simulations (see Figure 5 and Section 4.1). The thermal gradient promotes rainfall propagation into the city under a calm synoptic environment. The missing pockets of rainfall within the city consequently deteriorate the statistics of model evaluation for the two BEP simulations, especially the BEP_TAB simulation. The UCM_TAB simulation stands out with the best model performance for the 30 June 2018 storm (Figure 11f). Evaluation of the model performance is consistent among different evaluation statistics (see Table 6 for more details).

Despite the contrasts in spatial distributions of accumulated rainfall, time series of hourly rain rates averaged over model grids (for those that contain at least one rain gauge) are generally in good agreement among simulations, especially for the 10 June 2017 storm (Figure 12a). The simulated time series of hourly rainfall is consistent with the gauge observations. Correlation coefficients exceed 0.85 for all five simulations, with the largest value of 0.89 for the BEP_TAB simulation for the 10 June 2017 storm. The peak timing of the hourly rain rate is slightly different across the simulations for the 30 June 2018 storm, with the two BEP simulations presenting earlier peaks and larger peak magnitudes than the two UCM simulations. However, the UCM_TAB simulation shows the smallest biases of all five simulations, compared to the observed time series (Figure 12b). Model comparisons on the time series of hourly rain rates show consistent results with the evaluation on the spatial distribution of rainfall accumulation.

Based on the model evaluation statistics for the two storm events, we are unable to determine the added benefits of WRF simulations with multi-layer urban parametrization and/or updated UCPs in capturing spatial and temporal rainfall variability. In addition, the utility of incorporating the gridded UCPs seems to vary with storm events and urban parametrizations. For instance, the BEP_UCP simulation significantly reduces rainfall biases for the 30 June 2018 storm compared to the BEP_TAB simulation, but the improvement is not quite clear for the 30 June 2017 storm. The differences between the UCM_TAB and UCM_UCP simulations are relatively small, compared to those between the two BEP simulations (Figures 10f and 11f).

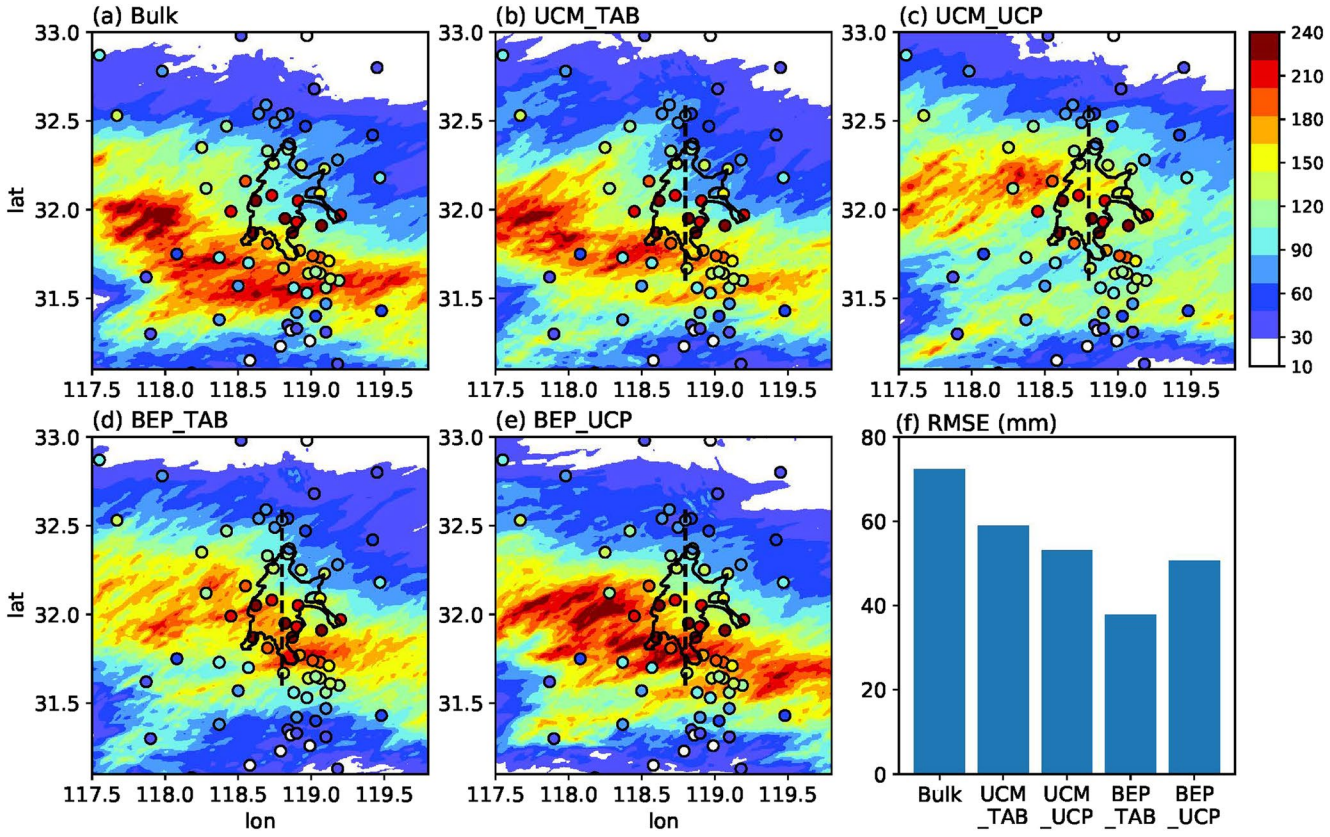

Figure 10. Maps of accumulated rainfall (in mm) in five different simulations (a–e) for the 10 June 2017 storm. Dots in the map represent gauge-based rainfall observations. The bar plot in (f) shows the RMSE of rainfall accumulations between all rain gauges and the corresponding model grids. The dashed line shows the position of cross-section for the vertical profile of moisture flux (see Figure 13).

The results are different from the contrasts in surface temperature and wind fields across simulations (see Section 4.1 for details), indicating the varied importance of thermal and dynamical fields across rainfall events. We will further explore the mechanisms responsible for rainfall variabilities in the following subsection, with a focus on the impacts of the urban canopy.

Table 6
Gauge-Based Statistics of Model Evaluation in Storm-Total Rainfall Accumulation for Both Events

	10 June 2017					30 June 2018				
	RMSE	Bias	CC	CSI	TSS	RMSE	Bias	CC	CSI	TSS
BULK	72.27	60.82	0.27	0.76	0.18	16.72	13.21	0.33	0.39	−0.09
UCM_TAB	58.84	47.31	0.47	0.83	0.36	13.55	10.17	0.50	0.48	0.21
UCM_UCP	52.94	41.98	0.56	0.83	0.32	17.73	13.68	0.17	0.43	−0.18
BEP_TAB	37.75	28.87	0.81	0.84	0.48	26.73	18.70	−0.28	0.36	−0.18
BEP_UCP	50.55	42.21	0.67	0.80	0.38	17.93	13.39	0.08	0.42	−0.24

Notes. Bias and "CC" represents mean bias (in mm) and correlation coefficient between rain-gauge observations and simulations at the corresponding model grids, respectively. Critical Success Index (CSI) and True Skill Statistic (TSS) are computed based on the contingency table indicating hit rate (a), false alarm rate (b), miss rate (c), and correct negative rate (d). CSI is defined as $\frac{a}{a+b+c}$, while TSS as $\frac{a}{a+b}+\frac{d}{d+c}-1$. Different rainfall thresholds are adopted for the two events, that is, 50 mm for the 2017 storm and 5 mm for the 2018 storm. See the texts for details about each scenario.

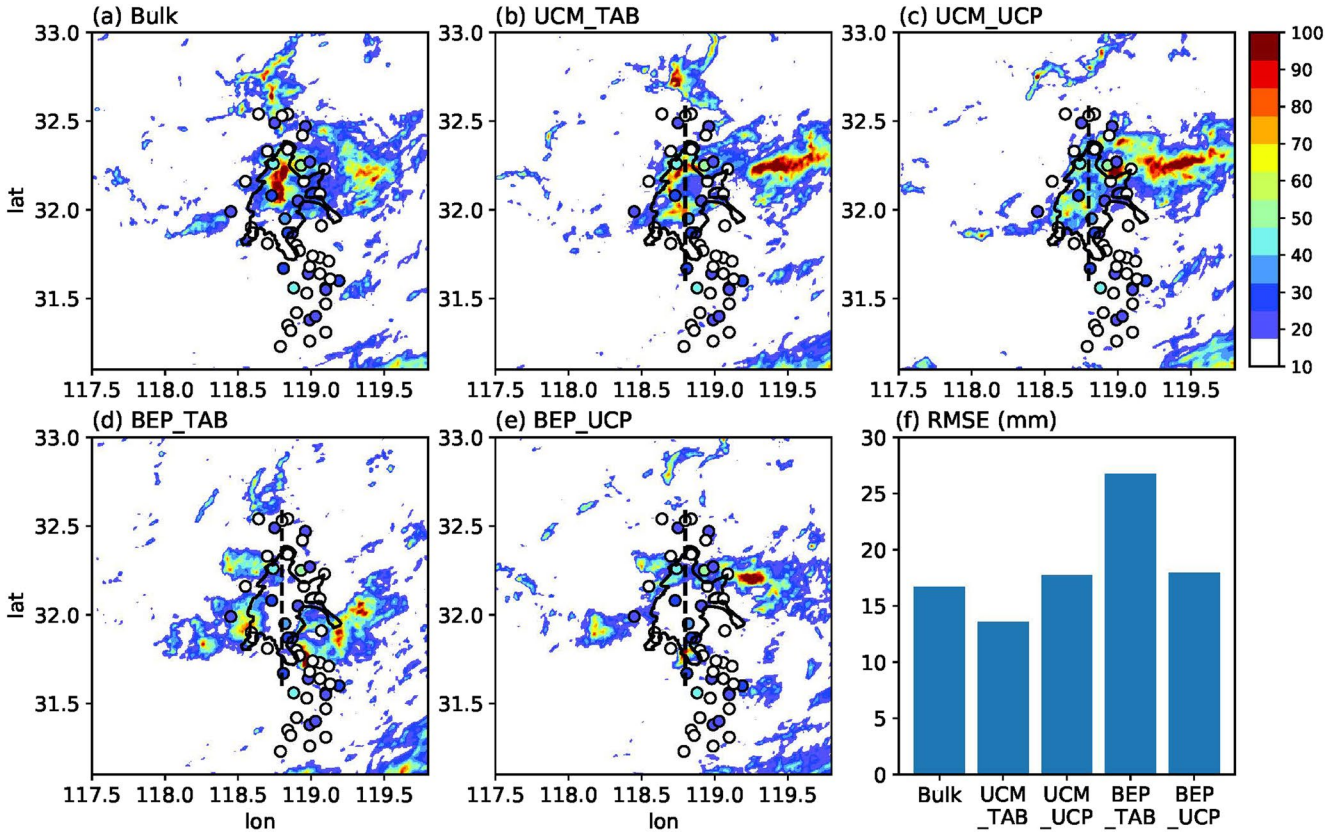

Figure 11. Same as Figure 10, but for the 30 June 2018 storm.

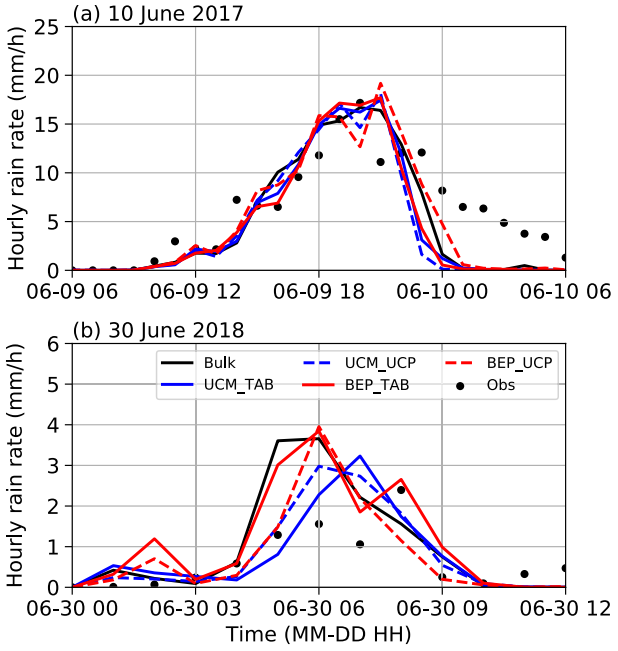

Figure 12. Time series of hourly rain rate (in mm/h) averaged over rain gauges and the corresponding model grids in different simulations for the (a) 10 June 2017 and (b) 30 June 2018 storm, respectively. Black dots show gauge-based observations.

4.3. Impacts of Urban Canopy on Rainfall Accumulation

We show vertical profiles of moisture flux and wind fields in Figure 13 to further highlight the differences in rainfall variabilities. The 10 June 2017 storm is characterized by a strong shear environment (also indicated by the sounding profile of wind speeds shown in Figure 7a), with southwesterly moist flow dominating the lower to middle levels of the atmosphere. A noticeable contrast across the simulations is the enhanced vertical velocity near the southern boundary (i.e., in the upwind direction) of the city in the two BEP simulations (Figures 13c and 13d), indicative of strong convergence induced by the urban canopy over the urban-rural interface. We can also identify enhanced convection over the city center in the two BEP simulations, compared to the two UCM simulations. The enhanced convection is mainly due to increased surface roughness over the city that decelerates wind speeds (Figure 8), which leads the convergence zone to expand from the urban-rural interface toward the city center. The thermal influence is limited, as contrasts in surface temperature are quite small across different simulations (Figure 6). The 30 June 2018 storm is characterized by weak synoptic forcing, with moisture advected into the city through near-surface vertical layers. The advection of moisture flux in the two UCM simulations is twice as strong as the two BEP simulations (the northern boundary of the city, see Figures 13e–13h). This is mainly because storm cells are bifurcated around the city in the two BEP simulations, as will be analyzed below.

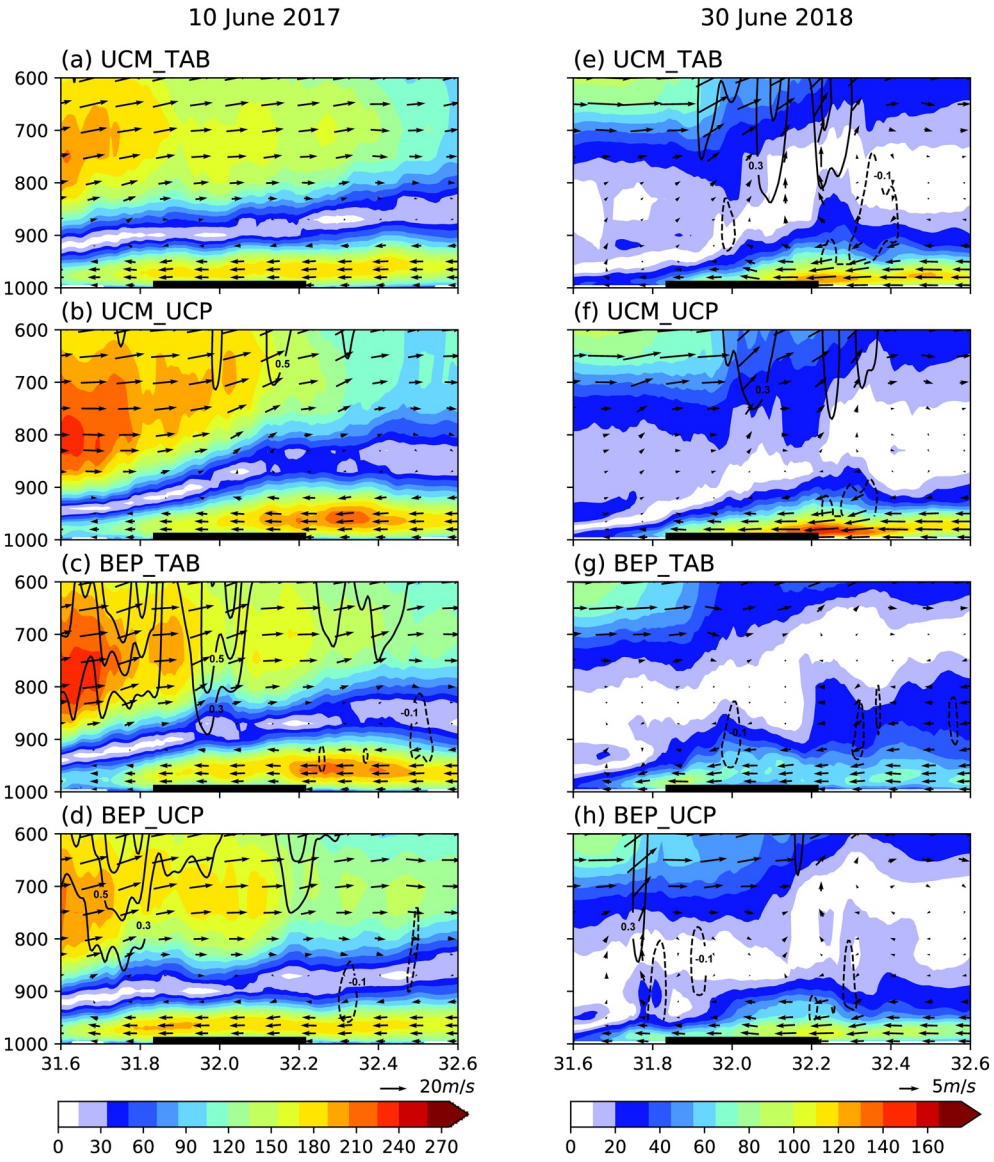

Figure 13. Vertical profiles of averaged moisture flux (shade, calculated as $Q_{vapor} \times \sqrt{V^2 + W^2}$), in m s^{-1} g kg^{-1}) and compound wind vectors (in v and w direction, in m/s) over the storm period along the cross-section shown in Figures 10 and 11a–11d, UTC on 09 June 2017 to 0400 UTC on 10 June 2017, (e–h), 1200 UTC–1600 UTC on 30 June 2018 for the sounding station and the corresponding model grid. The black contours show vertical velocity. The black horizontal line on the *x*-axis shows the urban extent.

Differences in rainfall accumulation between the two UCM and BEP simulations and the BULK simulation are shown in Figures 14 and 15. For both the 10 June 2017 and the 30 June 2018 storm, contrasts in accumulated rainfall between the four simulations and the BULK simulation are generally comparable, although they show considerable variance in magnitudes. The overestimation (underestimation) of rainfall accumulation over (outside) the city for the 2017 storm is tied to the fact that increased surface roughness (represented by either the UCM or BEP parametrization) enhances vertical wind shear and convergence, which subsequently increase the spatial contrast of rainfall. For the 2018 storm, the accumulated rainfall within the city is smaller in the four simulations (especially for the two BEP simulations) than in the BULK simulation (Figure 15). The "underestimated" rainfall accumulation might be partially associated with lower surface temperatures over the city in the four simulations compared to the BULK simulation (see Figures 5 and 6 for details), which reduces the intensity of moisture advection into the city. In addition,

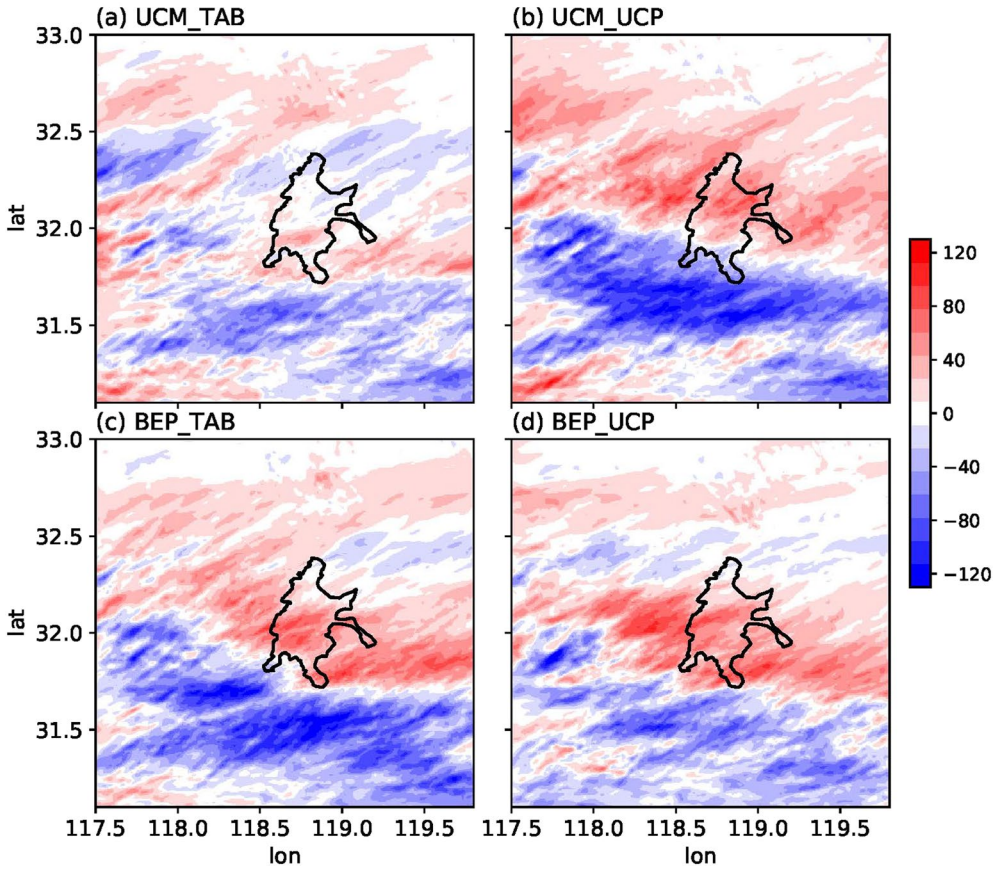

Figure 14. Differences of accumulated rainfall (in mm) between the (a) UCM_TAB, (b) UCM_UCP, (c) BEP_TAB, and (d) BEP_UCP simulation and the BULK simulation for the 10 June 2017 storm. The black line shows the boundary of Nanjing.

surface roughness over the city is much smaller in the BULK simulation than in either the UCM or BEP simulations that lead to larger surface wind speeds (see Figure 9). We consequently see that the storms tend to accumulate around the urban-rural interface in the UCM and BEP simulations rather than penetrating the city (see also Figure 11).

We further separate the interactive effects of urban parameterization and improved geometrical representation of urban canopy (as represented by the upgraded UCPs) based on the Factor Separation analysis approach (Stein & Alpert, 1993). Four scenarios are needed to separate two dependent factors. The UCM_TAB simulation is regarded as the baseline scenario (f_0), while the UCM_UCP simulation (f_1) and BEP_TAB simulation (f_2) represent the scenario with only one factor changed for each time. The BEP_UCP simulation (f_{12}) represents the scenario by changing both factors compared to the baseline scenario. The interactive effects are defined using the following formula, that is, (BEP_UCP-UCM_UCP)-(BEP_TAB-UCM_TAB). Figure 16 shows the spatial distributions of rainfall anomalies induced by the interactive effects for both storm events. A consistent finding is that there are strong positive rainfall anomalies over the upwind urban-rural interfaces, that is, over the southern boundary of the city for the 10 June 2017 storm and the northern boundary of the city for the 30 June 2018 storm. The magnitudes of positive rainfall anomalies are even comparable to the storm-total rainfall (see Figures 10 and 11 for comparisons). For instance, the largest rainfall anomalies for the 30 June 2018 storm induced by the interactive effects of building complexes are around 100 mm, comparable to the simulated storm-total rainfall (Figure 11). The largest rainfall anomalies for the 10 June 2017 storm can exceed 60% of the simulated storm-total rainfall (Figure 10).

Rainfall anomalies over the upwind urban-rural interfaces are closely tied to the perturbations of the urban canopy on atmospheric boundary layer processes and moisture transport. There is a moisture convergence

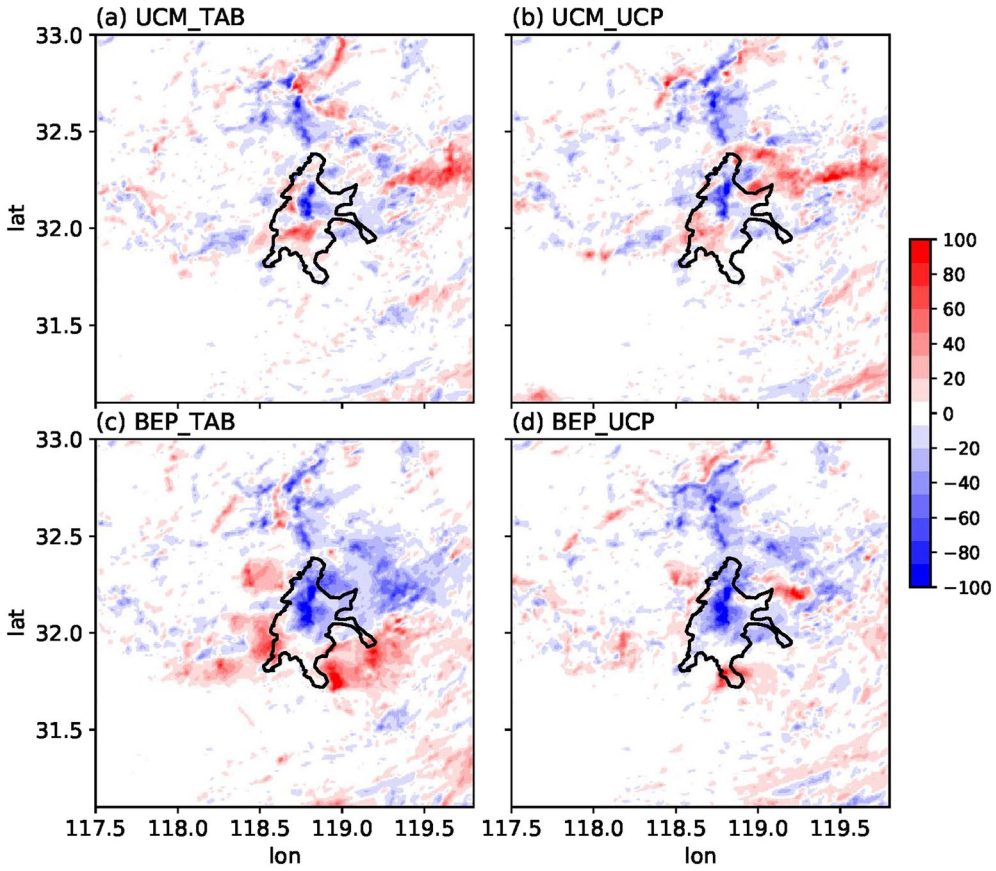

Figure 15. Same as Figure 14, but for the 30 June 2018 storm.

zone to the southern boundary of the city, in accompany with strong ascending air motion below 850 hPa at 00 UTC on 10 June 2017 (i.e., before the rainfall peak, Figure 17a). The convergence region highlights the blocking effect of the urban canopy in dictating low-level moisture transport in complex urban environments. There is also a moisture convergence zone outside the city boundary (in the upwind direction) along the cross-section A'B' for the 30 June 2018 storm (Figure 17b). The moisture convergence subsequently

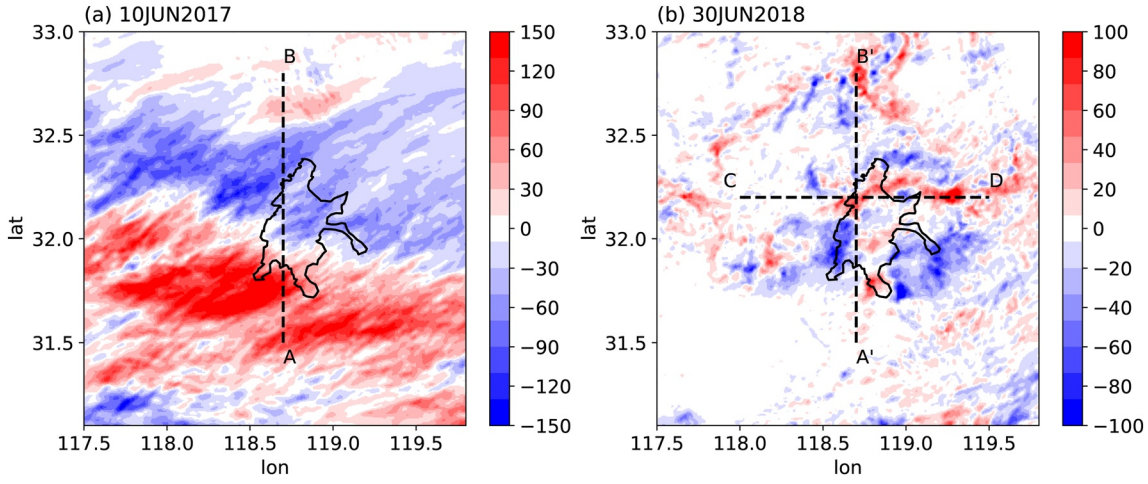

Figure 16. Anomalies in accumulated rainfall (in mm) induced by interactions between multi-layer urban parameterization and gridded UCPs for the (a) 10 June 2017 and (b) 30 June 2018 event, respectively. The black line shows the boundary of Nanjing.

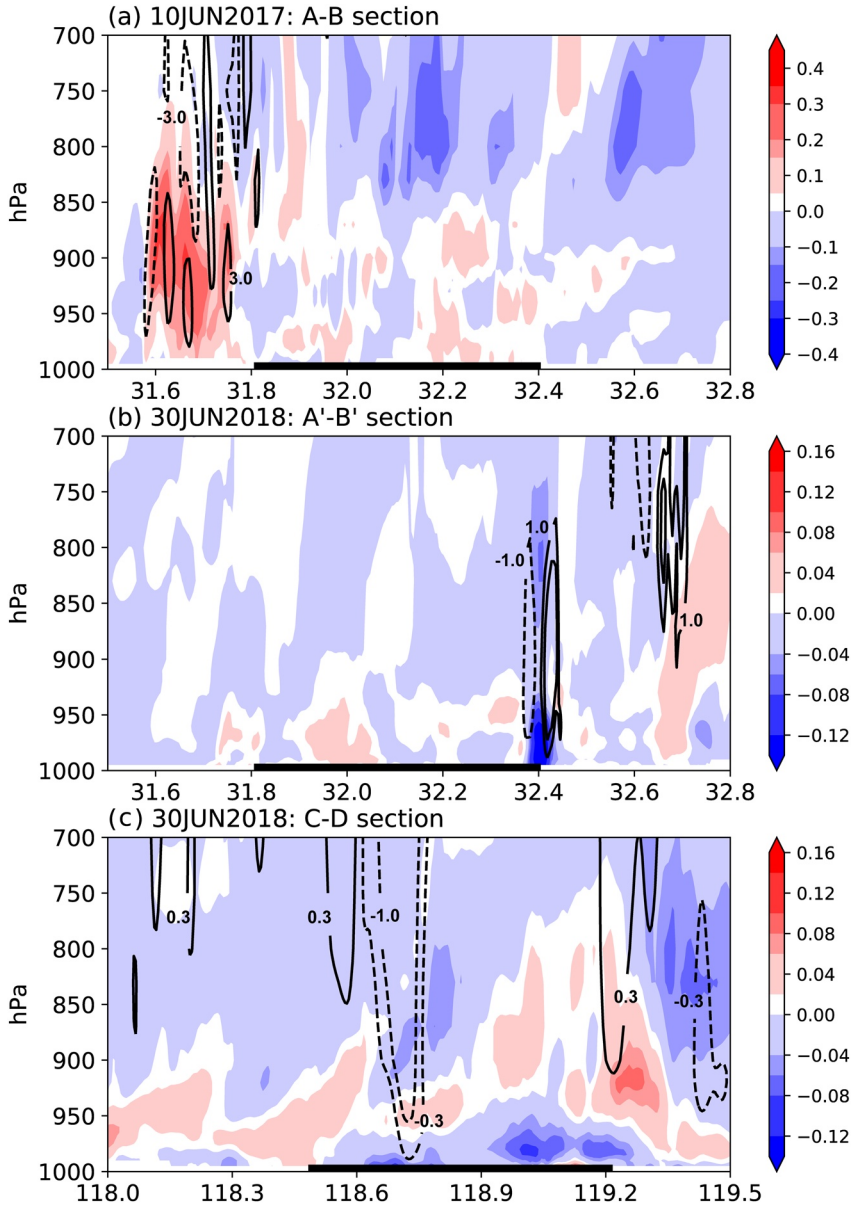

Figure 17. Cross-sections for the (a) 10 June 2017 storm (at 0000 UTC, along line AB, see location in Figure 16a). Vertical velocity is shown in black contours (dashed: −3 m/s, solid: 3 m/s), (b) 30 June 2018 storm (at 1200 UTC, along line A'B', see location in Figure 16b). Vertical velocity is shown in black contours (dashed: −1 m/s, solid: 1.0 m/s), and (c) 30 June 2018 storm (at 1200 UTC, along line CD, see location in Figure 16b). Vertical velocity is shown in black contours (dashed: −1 m/s, −0.3 m/s, solid: 1.0 m/s). The black horizontal line on the *x*-axis shows the urban extent. Color shading represents the moisture flux (in m s^{-1} kg kg^{-1}).

leads to bifurcated moisture flux along with the urban-rural interface rather than penetrating the city as the 10 June 2017 storm. As can be seen from the cross-section CD, there is a "triangular-shaped" region of negative anomalies in moisture flux over the northern boundary of the city for the 30 June 2018 storm at 1200 UTC (before the rainfall peak, Figure 17c). The positive anomalies of moisture transport lie above the "triangular-shaped" region and extend to both sides (the western and eastern side) of the city. The "triangular-shaped" region indicates the role of the urban canopy in modifying low-level ambient flows through the drag effects and vertical turbulent mixing. The bifurcated moisture fluxes are consequently responsible for the enhanced rainfall outside the city for the 30 June 2018 storm (see Figure 11c for details). We schematically summarize the contrasting mechanisms responsible for the spatial rainfall accumulation between the

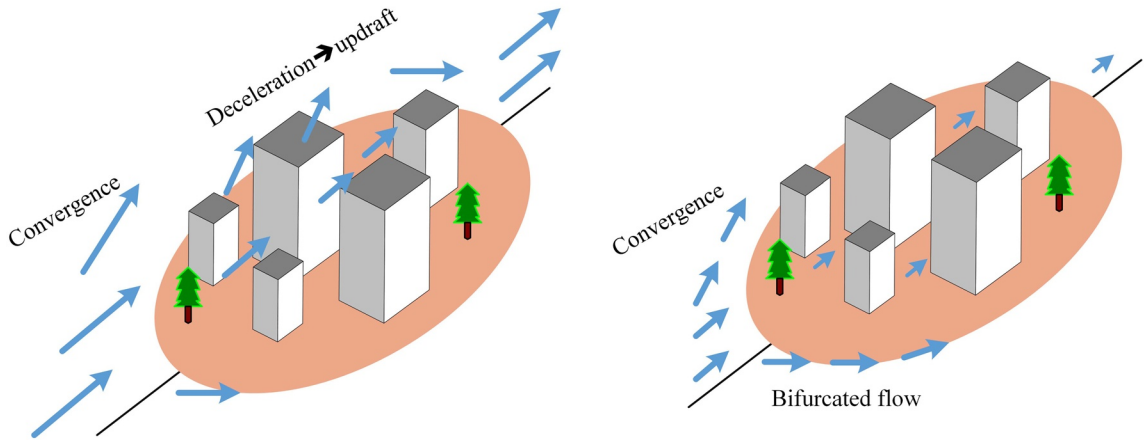

Figure 18. Schematic illustration of the role of the urban canopy in dictating spatial rainfall distribution for the two storms under contrasting synoptic conditions.

two storms in Figure 18. Although urban thermal influences might also have played a role in the rainfall patterns, we highlight that the impacts of the urban canopy (mainly through increasing surface roughness over the city) dominate rainfall contrasts across the simulations. The contrasts in rainfall accumulation are quite similar to those shown in low-level wind fields (Figures 8 and 9).

4.4. Storm Tracking Analysis for the 30 June 2018 Storm

We further carry out storm tracking analysis for the 30 June 2018 storm and provide a Lagrangian perspective of convective activities subject to local urban forcing. Storm tracking analysis is motivated by the comparisons of spatial rainfall patterns in the previous subsection that indicate the extremely heterogeneous nature of storm locations. Figure 19 shows the dominant complex tracks that are responsible for storm-total rainfall for the 30 June 2018 storm. A notable finding is that the storm tracks are deflected to the northern portion of the city according to the results of the two BEP simulations, while for the two UCM simulations and the BULK simulation, the storm cells are able to penetrate into the downtown region and produce extreme rainfall over the city. This is closely associated with the bifurcated moisture flux over the urban-rural interface as shown in Figure 17b. We also note that different urban representations (i.e., with or without gridded UCPs) lead to contrasts in storm evolution (Figures 19d and 19e), emphasizing the importance of urban canopy in dictating spatial rainfall variabilities in urban environments.

There is a relatively larger percentage of complex storm tracks (i.e., referring to storms that have splits and merges during the entire life cycle of the storm track) for the BEP_TAB (22%) and BEP_UCP simulation (19%), compared to 14%, 15%, and 17% for the BULK, UCM_TAB, and UCM_UCP simulation, respectively. In addition, the two BEP simulations seem to produce more storm cells with higher echo top heights and maximum reflectivity values, but smaller storm sizes and slower storm motion over the entire inner domain (Figure 20). Contrasts in storm structure and evolution properties among the five simulations become even sharper by zooming into the urban domain (see the black box in Figure 1). A notable finding is that the contrasts between two BEP simulations are larger than those between the two UCM simulations. The changing storm structure and evolution properties can directly lead to increased rainfall variabilities over cities (similarly see, e.g., Paul et al., 2018). A related question to explore in the future is to determine the extent of "influence domain" beyond which structure and evolution properties of storm cells are not clearly dictated by the local-scale urban forcings, for instance, the impacts of city size on storm structure and evolution (Kingfield et al., 2018; Lorenz et al., 2019; Schmid & Niyogi, 2013). Attention should also be paid to the vertical dimension of the "influence domain". This can be achieved through further examining the interactions between storm elements and atmospheric boundary layer processes in future studies.

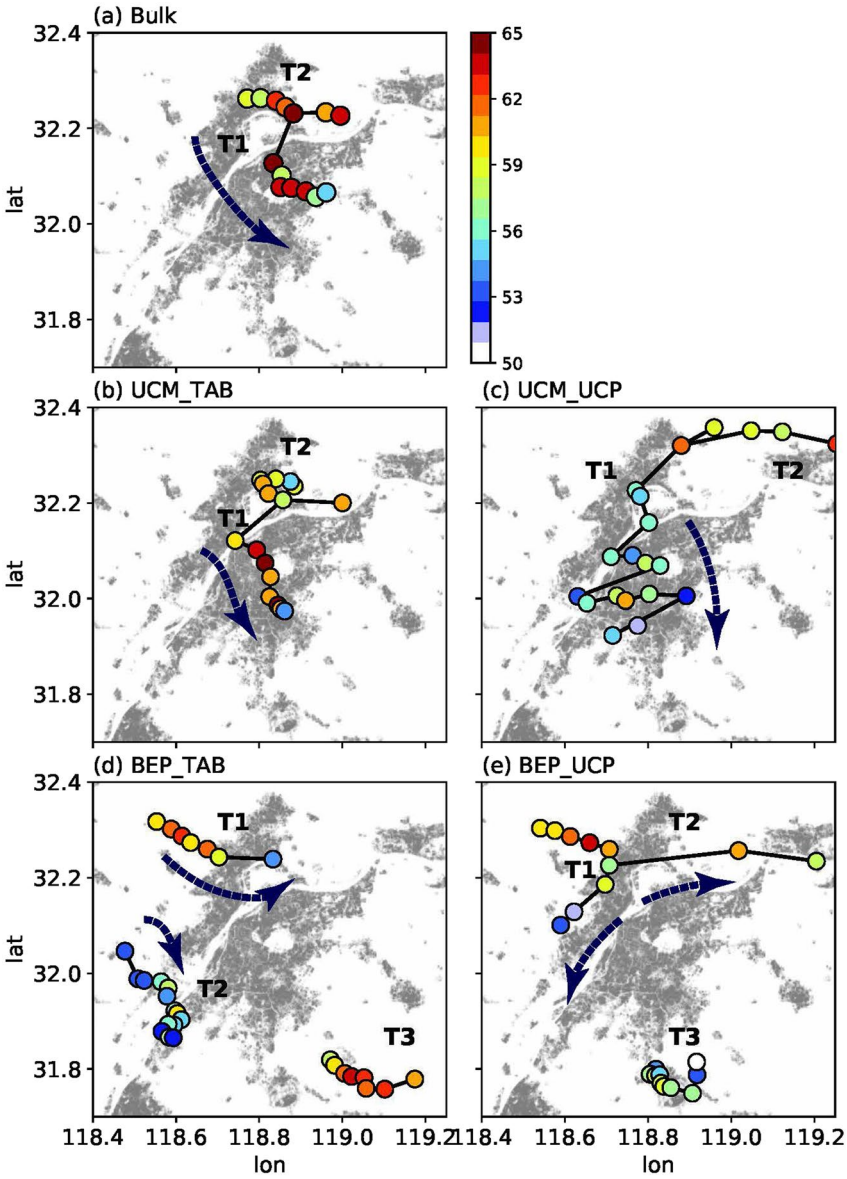

Figure 19. Dominant complex storm tracks (scatter and the dashed arrows) in the urban domain (see location in Figure 1) in different simulations during the period 1000 UTC–1500 UTC on 30 June 2018. Dots represent the centroid locations of individual storm cells in the storm track, with colors representing maximum reflectivity. The direction of the storm track is highlighted in blue arrows. Gray shading highlights impervious coverage over the entire region.

5. Summary and Conclusions

In this study, we examined the impacts of the urban canopy on the spatial and temporal rainfall variabilities for two convective rainfall events with contrasting synoptic conditions over Nanjing, China. A high-resolution, gridded dataset of UCPs was developed and incorporated into the WRF/Urban modeling system to represent the complex geometrical features of the urban canopy over Nanjing. Sensitivity simulations were designed and implemented to explicitly investigate the capacities of the WRF/Urban modeling system with different urban parametrizations and representations of the urban canopy in capturing spatial-temporal variabilities of convective rainfall. The main findings are summarized below.

(1) Gauge-based analyses of hourly rainfall observations during the warm seasons (May to September) of 2013–2017 show striking concentrations of extreme rainfall over downtown Nanjing, in terms of both intensity and frequency of extreme hourly rain rates. The hourly rain rates of the 99th percentile exceed

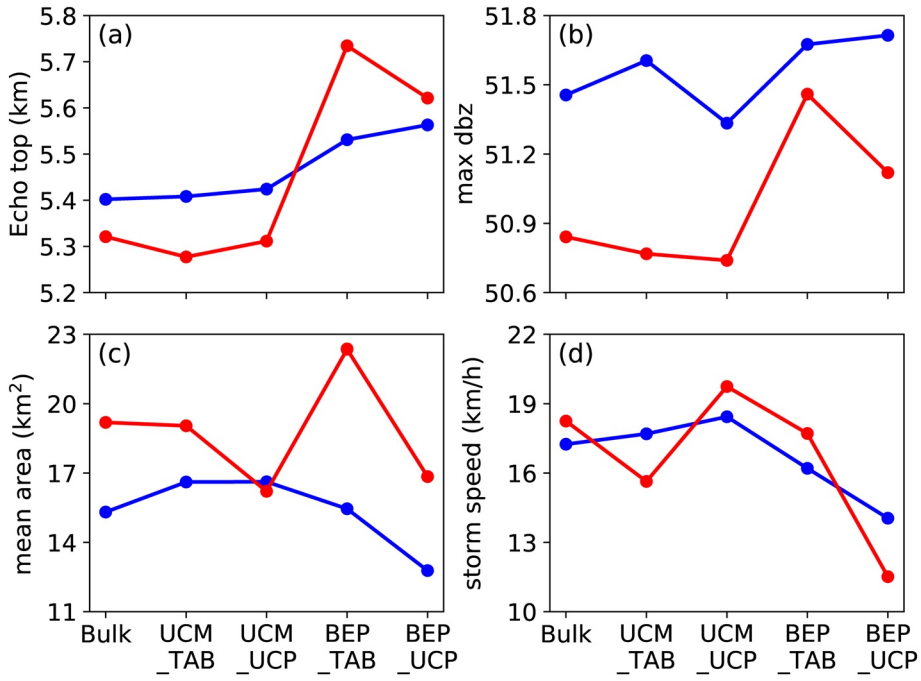

Figure 20. The averaged values of storm structure and evolution properties: (a) echo top height (in km), (b) maximum reflectivity (in dBZ), (c) storm size (in km^2), and (d) storm speed (in km/h) over domain 3 (in blue) and urban domain (in red, see Figure 1 for location). The statistics are based on all storm cells during the period 1000 UTC–1500 UTC on 30 June 2018.

28 mm/h for three gauges located in downtown and urban-rural interface, respectively. There are 28 h in total with rain rates exceeding 20 mm/h, which is about 3–4 times larger than its surrounding area. The number of hours sharply decreases to 7.5 h within approximately 50 km away from downtown, indicating a signature of urban impacts on convective rainfall over Nanjing.

(2) The WRF/Urban modeling system with the multi-layer urban parametrization (i.e., the BEP_TAB and BEP_UCP simulations) reduces simulation biases in 2-m air temperature for both storm events. The improvement in model performance is especially noticeable in the urban domain that is incorporated with gridded UCPs representing the geometrical features of the urban canopy. Despite the varied results in the station-level evaluation statistics, all five simulations produce comparable spatial patterns of surface temperature, for example, the urban-rural contrasts, for the two storm events. Contrast in simulated 2-m air temperature, surface heat fluxes, and near-surface wind fields among different simulations highlight the importance of accurate urban canopy representations in capturing thermodynamics and dynamics during convective rainfall events.

(3) Spatial distributions of accumulated rainfall for both storms show strong sensitivities to different urban representations in the WRF/Urban modeling system. The simulations with the multi-layer urban parametrization (i.e., the BEP_TAB and BEP_UCP simulations) better capture the spatial distribution of accumulated rainfall for the 10 June 2017 storm characterized by strong synoptic forcing. The single-layer urban physics (i.e., the UCM_TAB and UCM_UCP simulations) shows better performance for the 30 June 2018 storm. The deteriorated model performance of the two BEP simulations for 30 June 2018 is possibly tied to strong sensitivities of storm structure and evolution to local urban forcing under weak synoptic conditions. Contrasts in the simulated rainfall variabilities highlight that the utility of incorporating the gridded UCPs tends to vary with storm events and urban canopy parametrizations.

(4) Rainfall anomalies over the urban-rural interface are induced by the interactions of building complexes (as represented by the multi-layer urban parametrization) and improved representation of urban canopy based on the gridded UCPs for both storm events. The magnitudes of positive rainfall anomalies range from 60% to 100% of the storm-total rainfall. The rainfall anomalies are closely tied to the strong convergence of moisture flux over both the city boundary and city center for the 10 June 2017 storm and

bifurcating moisture flux around the city for the 30 June 2018 storm. Different behaviors of moisture transport between the two storms are tied to contrasting synoptic conditions. These results point to the critical role of the urban canopy and the perturbed atmospheric boundary layer processes in determining urban impacts on convective rainfall.

(5) Structure and evolution properties of convective storm cells are dictated by different urban representations in the WRF/Urban modeling system for the 30 June 2018 event. The dictation is especially noticeable in the vicinity of the city (i.e., urban domain), but shows relatively weaker contrasts when the domain of analysis expands far beyond the city (i.e., the entire innermost domain). Contrasting storm tracks clearly demonstrate the role of the urban canopy in deflecting convective storm cells under the weak synoptic condition when the storm approaches the city.

An important implication of our study is that urban signatures in convective rainfall vary depending on storm events. This echoes with Yang et al. (2019), among others, that shows contrasting spatial rainfall anomalies for two back-to-back storm episodes over the Phoenix metropolitan region in Arizona. While previous studies (e.g., Yang et al., 2019) focus on the collective impacts of urban coverages (i.e., based on contrasting simulations by removing cities from the model), the present study investigates the impacts of the urban canopy on spatial and temporal rainfall variabilities for storm events with contrasting synoptic conditions. The rainfall anomalies are slightly different for the two storms (Figures 14 and 15). Our results emphasize the importance of flow-regime analysis (i.e., synoptic conditions) in urban rainfall modification studies, although additional rainfall cases are required to further generalize the findings obtained in this study.

Investigation of urban rainfall modification is of paramount importance not only to scientific communities that seek improved understanding of the physical mechanisms of extreme rainfall in complex urban environments. Knowledge learned from this type of research serves as an indispensable pathway toward improved practices for urban flood forecasting and preparation as well as adaptation strategies for hazards related to extreme rainfall in cities (Yang, Tian, & Niyogi, 2015). While numerical simulations with updated urban parametrizations and/or improved representations of the urban canopy have shown noticeable benefits in characterizing surface thermodynamics, few studies have explored their utilities in examining convective rainfall in complex urban environments. The uncertainties in rainfall simulations can be attributed to multiple sources (e.g., Gilmore et al., 2004; Koch et al., 2005; Li et al., 2013; Yu et al., 2018). Our study presents the first evaluation of how spatial and temporal rainfall variabilities behave in response to different geometrical representations of the urban canopy. The utility of gridded UCPs plays a critical role in the multi-layer urban parametrization. Since the vector-format archive for urban buildings only covers the downtown region, the uncertainty may be related to the data itself. The World Urban Database and Access Portal Tool (WUDAPT), an ongoing effort that aims to remediate this conundrum by characterizing urban surfaces based on the Local Climate Zones, is unfortunately only available for a limited number of cities (Ching et al., 2018).

In addition, uncertainties in urban surface parameterizations as well as the reliability of the planetary boundary layer schemes certainly warrant further investigations for urban convective rainfalls (e.g., Patel et al., 2020). Apart from resolving the urban surface heterogeneity in the WRF modeling framework coupled with large-eddy simulations using the immerse boundary method (e.g., Auguste et al., 2019; Ma & Liu, 2017; Wiersema et al., 2020), another possible approach is to better resolve the urban boundary layer processes (via large-eddy simulations, e.g., Huang et al., 2019) for convective rainfall, and then explore the reliability of existing urban parametrizations in capturing the interactions between urban canopy and convective processes in atmospheric boundary layers.

Future studies should further investigate the influence of urban surface heterogeneities on land surface-atmosphere interactions in complex urban environments. For instance, Yang, Niyogi, et al. (2016) found contrasting impacts of urban forms (i.e., single-centric vs. multi-centric) on the thermal environment over Beijing, with a multi-centric city demonstrating a larger regional warming potential than a single-centric city. The contrasting influences can pass onto spatial and temporal rainfall variabilities. Analyses of such can further improve our understandings on the hydrometeorological impacts of urbanization and provide a foundation to increase the resilience of future cities to weather/climate-related hazards.

Data Availability Statement

The datasets for this research are available in https://doi.org/10.6084/m9.figshare.12187095, including rain-gauge observations, temperature observations, and sounding profiles.

Acknowledgments
This study is financially supported by the Natural Science Foundation of Jiangsu Province (SBK20190314), the Fundamental Research Funds for the Central Universities (0209-14380076) and the National Natural Science Foundation of China (42075187, 52009055). LY also acknowledges support of Open Research Fund Program of State Key Laboratory of Hydroscience and Engineering of Tsinghua University (SKLHSE-2020-A-02). QL acknowledges support of the startup fund from Cornell University and the small allocation grant for new faculty from the National Center for Atmospheric Research (CU00029) and National Science Foundation (NSF-AGS 2028644, NSF-CBET 2028842). The numerical simulations in this paper have been done on the computing facilities in the High Performance Computing Center (HPCC) of Nanjing University. Special thanks go to Dr. Mary Lynn Baeck from Princeton University for the scripts of pre-processing storm tracking analyses and Jie Wang from Nanjing University for the pre-selection of rainfall events.

References

Auguste, F., Réa, G., Paoli, R., Lac, C., Masson, V., & Cariolle, D. (2019). Implementation of an immersed boundary method in the Meso-NH v5.2 model Applications to an idealized urban environment. *Geoscientific Model Development*, *12*(6), 2607–2633. https://doi.org/10.5194/gmd-12-2607-2019

Barlage, M., Miao, S., & Chen, F. (2016). Impact of physics parameterizations on high-resolution weather prediction over two Chinese megacities. *Journal of Geophysical Research - D Atmospheres*, *121*(9), 4487–4498. https://doi.org/10.1002/2015jd024450

Bornstein, R., & Lin, Q. (2000). Urban heat islands and summertime convective thunderstorms in Atlanta: Three case studies. *Atmospheric Environment*, *34*(3), 507–516. https://doi.org/10.1016/s1352-2310(99)00374-x

Bornstein, R. D., & LeRoy, G. (1990). Urban barrier effects on convective and frontal thunderstorms. *In The Fourth AMS Conference on Mesoscale Processes, Boulder*, CO (pp. 120–121).

Burian, S. J., & J. Ching, 2009: Development of gridded fields of urban canopy parameters for advanced urban meteorological and air quality models. Tech. rep., U.S. Environmental Protection Agency (p. 73).

Carter, M., Shepherd, J. M., Burian, S., & Jeyachandran, I. (2012). Integration of lidar data into a coupled mesoscale-land surface model: A theoretical assessment of sensitivity of urban-coastal mesoscale circulations to urban canopy parameters. *Journal of Atmospheric and Oceanic Technology*, *29*(3), 328–346. https://doi.org/10.1175/2011jtecha1524.1

Chang, C. P., Chan, J. C. L., & Wang, J. T. (1998). *East Asia and western Pacific meteorology and climate* (pp. 1–582). Taiwan. https://www.worldscientific.com/doi/pdf/10.1142/9789814530040

Changnon, S. A. (1975). The paradox of planned weather modification. *Bulletin of the American Meteorological Society*, *56*(1), 27–37. https://doi.org/10.1175/1520-0477(1975)056<0027:tpopwm>2.0.co;2

Changnon, S. A., Huff, F. A., & Semonin, R. G. (1971). METROMEX: An investigation of inadvertent weather modification. *Bulletin of the American Meteorological Society*, *52*(10), 958–968. https://doi.org/10.1175/1520-0477(1971)052<0958:maioiw>2.0.co;2

Chen, F., Kusaka, H., Bornstein, R., Ching, J., Grimmond, C. S. B., Grossman-Clarke, S., et al. (2011). The integrated WRF/urban modeling system: Development, evaluation, and applications to urban environmental problems. *International Journal of Climatology*, *31*(2), 273–288. https://doi.org/10.1002/joc.2158

Ching, J. (2013). A perspective on urban canopy layer modeling for weather, climate and air quality applications. *Urban Climate*, *3*, 13–39. https://doi.org/10.1016/j.uclim.2013.02.001

Ching, J., Brown, M., Burian, S., Chen, F., Cionco, R., Hanna, A., et al. (2009). National urban database and access portal tool. *Bulletin of the American Meteorological Society*, *90*(8), 1157–1168. https://doi.org/10.1175/2009bams2675.1

Ching, J., Mills, G., Bechtel, B., See, L., Feddema, J., Wang, X., et al. (2018). WUDAPT: An urban weather, climate, and environmental modeling infrastructure for the Anthropocene. *Bulletin of the American Meteorological Society*, *99*(9), 1907–1924. https://doi.org/10.1175/bams-d-16-0236.1

Debbage, N., & Shepherd, J. M. (2018). Urban influences on the spatiotemporal characteristics of runoff and precipitation during the 2009 Atlanta flood. *Journal of Hydrometeorology*, *20*(1), 3–21.

Ding, Y., & Chan, J. C. L. (2005). The East Asian summer monsoon: An overview. *Meteorology and Atmospheric Physics*, *89*(1), 117–142.

Ding, Y., & Zhang, J. (2009). *Torrential rains and flashing floods* (p. 290). Meteorological Press.

Dixon, M., & Wiener, G. (1993). TITAN: Thunderstorm identification, tracking, analysis, and now casting—a radar-based methodology. *Journal of Atmospheric and Oceanic Technology*, *10*, 785–797. https://doi.org/10.1175/1520-0426(1993)010<0785:ttitaa>2.0.co;2

Dixon, P. G., & Mote, T. L. (2003). Patterns and causes of Atlanta's urban heat island-initiated precipitation. *Journal of Applied Meteorology*, *42*(9), 1273–1284. https://doi.org/10.1175/1520-0450(2003)042<1273:pacoau>2.0.co;2

Dou, J., Wang, Y., Bornstein, R., & Miao, S. (2015). Observed spatial characteristics of Beijing urban climate impacts on summer thunderstorms. *Journal of Applied Meteorology and Climatology*, *54*(1), 94–105. https://doi.org/10.1175/jamc-d-13-0355.1

Freitag, B. M., Nair, U. S., & Niyogi, D. (2018). Urban modification of convection and rainfall in complex terrain. *Geophysical Research Letters*, *45*(5), 2507–2515. https://doi.org/10.1002/2017gl076834

Gilmore, M. S., Straka, J. M., & Rasmussen, E. N. (2004). Precipitation uncertainty due to variations in precipitation particle parameters within a simple microphysics scheme. *Monthly Weather Review*, *132*(11), 2610–2627. https://doi.org/10.1175/mwr2810.1

Giovannini, L., Zardi, D., De Franceschi, M., & Chen, F. (2014). Numerical simulations of boundary-layer processes and urban-induced alterations in an alpine valley. *International Journal of Climatology*, *34*(4), 1111–1131. https://doi.org/10.1002/joc.3750

Gutierrez, E., Gonzalez, J. E., Bornstein, R., Arend, M., & Martilli, A. (2011). A new modeling approach to forecast building energy demands during extreme heat events in complex cities. *ASME 2011 5th International Conference on Energy Sustainability, Parts A, B, and C*, *135*, 1879–1884.

Gutiérrez, E., González, J. E., Martilli, A., Bornstein, R., & Arend, M. (2015). Simulations of a heat-wave event in New York City using a multilayer urban parameterization. *Journal of Applied Meteorology and Climatology*, *54*(2), 283–301. https://doi.org/10.1175/jamc-d-14-0028.1

He, X., Li, Y., Wang, X., Chen, L., Yu, B., Zhang, Y., & Miao, S. (2019). High-resolution dataset of urban canopy parameters for Beijing and its application to the integrated WRF/Urban modeling system. *Journal of Cleaner Production*, *208*, 373–383. https://doi.org/10.1016/j.jclepro.2018.10.086

He, X., Wang, J., Feng, J., Yan, Z., Miao, S., Zhang, Y., & Xia, J. (2020). Observational and modeling study of interactions between urban heat island and heatwave in Beijing. *Journal of Cleaner Production*, *247*, 119–169. https://doi.org/10.1016/j.jclepro.2019.119169

Huang, Y., Liu, Y., Liu, Y., Li, H., & Knievel, J. C. (2019). Mechanisms for a record-breaking rainfall in the coastal metropolitan city of Guangzhou, China: Observation analysis and nested very large eddy simulation with the WRF model. *Journal of Geophysical Research - D: Atmospheres*, *124*(3), 1370–1391. https://doi.org/10.1029/2018jd029668

Jiang, X., Luo, Y., Zhang, D.-L., & Wu, M. (2020). Urbanization enhanced summertime extreme hourly precipitation over the Yangtze River Delta. *Journal of Climate*, *33*(13), 5809–5826. https://doi.org/10.1175/jcli-d-19-0884.1

Jin, M., Shepherd, J. M., & King, M. D. (2005). Urban aerosols and their variations with clouds and rainfall: A case study for New York and Houston. *Journal of Geophysical Research: Atmospheres*, *110*(10), 1–12. https://doi.org/10.1029/2004jd005081

Kingfield, D. M., Calhoun, K. M., de Beurs, K. M., & Henebry, G. M. (2018). Effects of city size on thunderstorm evolution revealed through a multiradar climatology of the central United States. *Journal of Applied Meteorology and Climatology*, *57*(2), 295–317. https://doi.org/10.1175/jamc-d-16-0341.1

Koch, S. E., Segal, M., Shaw, B., Jankov, I., & Gallus, W. A. (2005). The impact of different WRF model physical parameterizations and their interactions on warm season MCS rainfall. *Weather and Forecasting*, *20*(6), 1048–1060.

Li, D., Bou-Zeid, E., Baeck, M. L., Jessup, S., & Smith, J. A. (2013). Modeling land surface processes and heavy rainfall in urban environments: Sensitivity to urban surface representations. *Journal of Hydrometeorology*, *14*(4), 1098–1118. https://doi.org/10.1175/jhm-d-12-0154.1

Liang, X., Miao, S., Li, J., Bornstein, R., Zhang, X., Gao, Y., et al. (2018). SURF: Understanding and predicting urban convection and haze. *Bulletin of the American Meteorological Society*, *99*(7), 1391–1413. https://doi.org/10.1175/bams-d-16-0178.1

Liao, J., Wang, T., Wang, X., Xie, M., Jiang, Z., Huang, X., & Zhu, J. (2014). Impacts of different urban canopy schemes in WRF/Chem on regional climate and air quality in Yangtze River Delta, China. *Atmospheric Research*, *145–146*, 226–243. https://doi.org/10.1016/j.atmosres.2014.04.005

Lin, C.-Y., Chen, W.-C., Chang, P.-L., & Sheng, Y.-F. (2011). Impact of the urban heat island effect on precipitation over a complex geographic environment in northern Taiwan. *Journal of Applied Meteorology and Climatology*, *50*(2), 339–353. https://doi.org/10.1175/2010jamc2504.1

Liu, J., & Niyogi, D. (2019). Meta-analysis of urbanization impact on rainfall modification. *Scientific Reports*, *9*, 7301. https://doi.org/10.1038/s41598-019-42494-2

Liu, X., Hu, G., Chen, Y., Li, X., Xu, X., Li, S., et al. (2018). High-resolution multi-temporal mapping of global urban land using Landsat images based on the Google Earth Engine Platform. *Remote Sensing of Environment*, *209*, 227–239. https://doi.org/10.1016/j.rse.2018.02.055

Lorenz, J. M., Kronenberg, R., Bernhofer, C., & Niyogi, D. (2019). Urban rainfall modification: Observational climatology over Berlin, Germany. *Journal of Geophysical Research - D: Atmospheres*, *124*(2), 731–746. https://doi.org/10.1029/2018jd028858

Ma, Y., & Liu, H. (2017). Large-eddy simulations of atmospheric flows over complex terrain using the immersed-boundary method in the weather research and forecasting model. *Boundary-Layer Meteorology*, *165*(3), 421–445. https://doi.org/10.1007/s10546-017-0283-9

McLeod, J., Shepherd, M., & Konrad, C. E. (2017). Spatio-temporal rainfall patterns around Atlanta, Georgia and possible relationships to urban land cover. *Urban Climate*, *21*, 27–42. https://doi.org/10.1016/j.uclim.2017.03.004

Miao, S., Chen, F., Li, Q., & Fan, S. (2011). Impacts of urban processes and urbanization on summer precipitation: A case study of heavy rainfall in Beijing on 1 August 2006. *Journal of Applied Meteorology and Climatology*, *50*(4), 806–825. https://doi.org/10.1175/2010jamc2513.1

Nie, W., Zaitchik, B. F., Ni, G., & Sun, T. (2017). Impacts of anthropogenic heat on summertime rainfall in Beijing. *Journal of Hydrometeorology*, *18*(3), 693–712. https://doi.org/10.1175/jhm-d-16-0173.1

Niyogi, D., Pyle, P., Lei, M., Arya, S. P., Kishtawal, C. M., Shepherd, M., et al. (2011). Urban modification of thunderstorms: An observational storm climatology and model case study for the Indianapolis urban region. *Journal of Applied Meteorology and Climatology*, *50*(5), 1129–1144. https://doi.org/10.1175/2010jamc1836.1

Patel, P., Karmakar, S., Ghosh, S., & Niyogi, D. (2020). Improved simulation of very heavy rainfall events by incorporating WUDAPT urban land use/land cover in WRF. *Urban Climate*, *32*. https://doi.org/10.1016/j.uclim.2020.100616

Paul, S., Ghosh, S., Mathew, M., Devanand, A., Karmakar, S., & Niyogi, D. (2018). Increased spatial variability and intensification of extreme monsoon rainfall due to urbanization. *Scientific Reports*, *8*(1), 1–10. https://doi.org/10.1038/s41598-018-22322-9

Reames, L. J., & Stensrud, D. J. (2018). Influence of a great plains urban environment on a simulated supercell. *Monthly Weather Review*, *146*(5), 1437–1462. https://doi.org/10.1175/mwr-d-17-0284.1

Rosenfeld, D. (2000). Suppression of rain and snow by urban and industrial air pollution. *Science*, *287*(5459), 1793–1796. https://doi.org/10.1126/science.287.5459.1793

Ryu, Y. H., Smith, J. A., Bou-Zeid, E., & Baeck, M. L. (2015). The influence of land surface heterogeneities on heavy convective rainfall in the Baltimore–Washington metropolitan area. *Monthly Weather Review*, *144*(2), 553–573.

Salamanca, F., Martilli, A., Tewari, M., & Chen, F. (2011). A study of the urban boundary layer using different urban parameterizations and high-resolution urban canopy parameters with WRF. *Journal of Applied Meteorology and Climatology*, *50*(5), 1107–1128. https://doi.org/10.1175/2010jamc2538.1

Salamanca, F., Zhang, Y., Barlage, M., Chen, F., Mahalov, A., & Miao, S. (2018). Evaluation of the WRF-Urban Modeling System Coupled to Noah and Noah-MP Land Surface Models Over a Semiarid Urban Environment. *Journal of Geophysical Research - D: Atmospheres*, *123*(5), 2387–2408. https://doi.org/10.1002/2018jd028377

Schmid, P. E., & Niyogi, D. (2013). Impact of city size on precipitation-modifying potential. *Geophysical Research Letters*, *40*(19), 5263–5267. https://doi.org/10.1002/grl.50656

Sharma, A., Fernando, H. J. S., Hamlet, A. F., Hellmann, J. J., Barlage, M., & Chen, F. (2017). Urban meteorological modeling using WRF: A sensitivity study. *International Journal of Climatology*, *37*(4), 1885–1900. https://doi.org/10.1002/joc.4819

Shen, C., Chen, X., Dai, W., Li, X., Wu, J., Fan, Q., et al. (2019). Impacts of high-resolution urban canopy parameters within the WRF model on dynamical and thermal fields over Guangzhou, China. *Journal of Applied Meteorology and Climatology*, *58*, 1155–1176. https://doi.org/10.1175/jamc-d-18-0114.1

Shepherd, J. M. (2005). A review of current investigations of urban-induced rainfall and recommendations for the future. *Earth Interactions*, *9*, 1–27. https://doi.org/10.1175/ei156.1

Shepherd, J. M. (2013). Impacts of urbanization on precipitation and storms: Physical insights and vulnerabilities. *Climate Vulnerability: Understanding and Addressing Threats to Essential Resources*, *5*, 109–125. https://doi.org/10.1016/b978-0-12-384703-4.00503-7

Skamarock, W., & Coauthors, (2019). A description of the advanced research WRF model Version 4. NCAR Technical Note NCAR/TN-475+STR, 145.

Stein, U., & Alpert, P. (1993). Factor separation in numerical simulations. *Journal of the Atmospheric Sciences*, *50*(14), 2107–2115. https://doi.org/10.1175/1520-0469(1993)050<2107:fsins>2.0.co;2

Templeton, N. P., Vivoni, E. R., Wang, Z.-H., & Schreiner-McGraw, A. P. (2018). Quantifying water and energy fluxes over different urban land covers in Phoenix, Arizona. *Journal of Geophysical Research - D: Atmospheres*, *123*(4), 2111–2128. https://doi.org/10.1002/2017jd027845

Vahmani, P., & Hogue, T. S. (2014). Incorporating an urban irrigation module into the Noah land surface model coupled with an urban canopy model. *Journal of Hydrometeorology*, *15*(4), 1440–1456. https://doi.org/10.1175/jhm-d-13-0121.1

Wiersema, D. J., Lundquist, K. A., & Chow, F. K. (2020). Mesoscale to microscale simulations over complex terrain with the immersed boundary method in the weather research and forecasting model. *Monthly Weather Review*, *148*(2), 577–595. https://doi.org/10.1175/mwr-d-19-0071.1

Wu, M., Luo, Y., Chen, F., & Wong, W. K. (2019). Observed Link of Extreme Hourly Precipitation Changes to Urbanization over Coastal South China. *Journal of Applied Meteorology and Climatology, 58*(8), 1799–1819. https://doi.org/10.1175/jamc-d-18-0284.1

Yang, J., Wang, Z.-H., Chen, F., Miao, S., Tewari, M., Voogt, J. A., & Myint, S. (2015). Enhancing hydrologic modeling in the coupled Weather Research and Forecasting-urban modeling system. *Boundary-Layer Meteorology*, *155*(1), 87–109. https://doi.org/10.1007/s10546-014-9991-6

Yang, J., Wang, Z.-H., Georgescu, M., Chen, F., & Tewari, M. (2016). Assessing the impact of enhanced hydrological processes on urban hydrometeorology with application to two cities in contrasting climates. *Journal of Hydrometeorology*, *17*(4), 1031–1047. https://doi.org/10.1175/jhm-d-15-0112.1

Yang, L., Niyogi, D., Tewari, M., Aliaga, D., Chen, F., Tian, F., & Ni, G. (2016). Contrasting impacts of urban forms on the future thermal environment: Example of Beijing metropolitan area. *Environmental Research Letters*, *11*(3). https://doi.org/10.1088/1748-9326/11/3/034018

Yang, L., & Smith, J. (2018). Sensitivity of extreme rainfall to atmospheric moisture content in the arid/semiarid southwestern United States: Implications for probable maximum precipitation estimates. *Journal of Geophysical Research - D: Atmospheres*, *123*(3), 1638–1656. https://doi.org/10.1002/2017jd027850

Yang, L., Smith, J., Baeck, M. L., Smith, B., Tian, F., & Niyogi, D. (2016). Structure and evolution of flash flood producing storms in a small urban watershed. *Journal of Geophysical Research - D: Atmospheres*, *121*(7), 3139–3152. https://doi.org/10.1002/2015jd024478

Yang, L., Smith, J., & Niyogi, D. (2019). Urban impacts on extreme monsoon rainfall and flooding in complex terrain. *Geophysical Research Letters*, *46*, 5918–5927. https://doi.org/10.1029/2019gl083363

Yang, L., Smith, J. A., Baeck, M. L., Bou-Zeid, E., Jessup, S. M., Tian, F., & Hu, H. (2014). Impact of urbanization on heavy convective precipitation under strong large-scale forcing: A case study over the Milwaukee-Lake Michigan Region. *Journal of Hydrometeorology*, *15*(1), 261–278. https://doi.org/10.1175/jhm-d-13-020.1

Yang, L., Tian, F., & Niyogi, D. (2015). A need to revisit hydrologic responses to urbanization by incorporating the feedback on spatial rainfall patterns. *Urban Climate*, *12*, 128–140. https://doi.org/10.1016/j.uclim.2015.03.001

Yang, L., Tian, F., Smith, J. A., & Hu, H. (2014b). Urban signatures in the spatial clustering of summer heavy rainfall events over the Beijing metropolitan region. *Journal of Geophysical Research - D: Atmospheres*, *119*(3), 1203–1217. https://doi.org/10.1002/2013jd020762

Yeung, J. K., Smith, J. A., Baeck, M. L., & Villarini, G. (2015). Lagrangian analyses of rainfall structure and evolution for organized thunderstorm systems in the urban corridor of the Northeastern United States. *Journal of Hydrometeorology*, *16*(4), 1575–1595. https://doi.org/10.1175/jhm-d-14-0095.1

Yu, M., & Liu, Y. (2015). The possible impact of urbanization on a heavy rainfall event in Beijing. *Journal of Geophysical Research - D: Atmospheres*, *120*, 8132–8143. https://doi.org/10.1002/2015jd023336

Yu, M., Miao, S., & Zhang, H. (2018). Uncertainties in the impact of urbanization on heavy rainfall: Case study of a rainfall event in Beijing on 7 August 2015. *Journal of Geophysical Research - D: Atmospheres*, *123*(11), 6005–6021. https://doi.org/10.1029/2018jd028444

Zhang, D. L. (2020). Rapid urbanization and more extreme rainfall events. *Science Bulletin*, *1*, 9–11.

Zhang, D.-L., Jin, M. S., Shou, Y., & Dong, C. (2019). The influences of urban building complexes on the ambient flows over the Washington-Reston region. *Journal of Applied Meteorology and Climatology*, *58*(6), 1325–1336. https://doi.org/10.1175/jamc-d-19-0037.1

Zhong, S., Qian, Y., Zhao, C., Leung, R., Wang, H., Yang, B., et al. (2017). Urbanization-induced urban heat island and aerosol effects on climate extremes in the Yangtze River Delta region of China. *Atmospheric Chemistry and Physics*, *17*(8), 5439–5457. https://doi.org/10.5194/acp-17-5439-2017